Observation and parameterization of bottom shear stress and sediment resuspension in a large shallow lake

S. Lin[1,3*], L. Boegman[1], A. Jabbari[2], R. Valipour[3], Y. Zhao[4]

1. Environmental Fluid Dynamics Laboratory, Queen's University, Kingston, ON, Canada, K7L 3N6

2. Fisheries and Oceans Canada, Bedford Institute of Oceanography, Dartmouth, NS, Canada, B2Y 4A2

3. Environment and Climate Change Canada, Canada Centre for Inland Waters, Burlington, ON, Canada, L7R 4A6

4. Aquatic Research and Monitoring Section, Ontario Ministry of Natural Resources and Forestry, Lake Erie Fishery Station, Wheatley, ON, Canada, N0P 2P0

* Corresponding author email: shuqi.lin@ec.gc.ca

Key Points:

- Three observation-based bottom shear stress parameterizations were assessed in a large shallow lake
- The parameterizations of bottom shear stress in Reynolds-averaged Navier-Stokes equation models was assessed against the observations

Abstract

Parameterizations for bottom shear stress are required to predict sediment resuspension from field observations and within numerical models that do not resolve flow within the viscous sublayer. This study assessed three observation-based bottom shear stress (τ_b) parameterizations, including (1) the sum of surface wave stress and mean current (quadratic) stress ($\tau_b = \tau_w + \tau_c$); (2) the log-law ($\tau_b = \tau_L$); and (3) the turbulent kinetic energy ($\tau_b = \tau_{TKE}$); using two years of observations from a large shallow lake. For this system, the parameterization $\tau_b = \tau_w + \tau_c$ was sufficient to qualitatively predict resuspension, since bottom currents and surface wave orbitals were the two major processes found to resuspend bottom sediments. However, the τ_L and τ_{TKE} parameterizations also captured the development of a nepheloid layer within the hypolimnion associated with high-frequency internal waves. Reynolds-averaged Navier-Stokes (RANS) equation models parameterize τ_b as the summation of modeled current-induced bottom stress ($\tau_{c,m}$) and modelled surface wave-induced bottom stress ($\tau_{w,m}$). The performance of different parameterizations for $\tau_{w,m}$ and $\tau_{c,m}$ in RANS models was assessed against the observations. The optimal parameterizations yielded root-mean-square errors of 0.031 and 0.025 Pa, respectively, when $\tau_{w,m}$, and $\tau_{c,m}$ were set using a constant canonical drag coefficient. A RANS-based τ_L parameterization was developed; however, the grid-averaged modelled dissipation did not always match local observations, leading to *O*(10) errors in prediction of bottom stress. Turbulence-based parameterizations should be further developed for application to flows with mean shear-free boundary turbulence.

Plain Language Summary

Bottom shear stress is the link between hydrodynamic motions and sediment resuspension, further relating to water quality in the lake. However, it is impractical to directly measure the

bottom shear stress in the field. We assessed three observation-based bottom shear stress parameterizations, using two years of observations from a large shallow lake, and found that the parameterization consisting of surface wave-induced stress and bottom current-induced stress is sufficient to capture major sediment resuspension events. In the numerical models, which averaged the turbulence dissipation, the parameterization based on modeled surface wave-induced stress and bottom current-induced stress was also assessed and compared against the values from observation-based parameterizations. The usage of a constant, observed or literature-based parameter in the model parameterization is recommended, and it should be calibrated to account for inaccuracies in modeled hydrodynamic variables (i.e., surface waves and bottom currents).

1. Introduction

1.1 Sediment resuspension and its mechanisms

Sediment resuspension, in shallow lakes and nearshore coastal regions, can contribute to total suspended solids (TSS), which is an important biogeochemical component in aquatic systems (e.g., Donohue and Molinos, 2009; Bruton, 1985; Valipour et al., 2017). Bottom shear stress (τ_b) drives resuspension and is, therefore, a link between hydrodynamic forcing and water quality (e.g., (Kim et al., 2000; Biron et al., 2004; Salim et al., 2018). Resuspension in the benthic boundary layer (BBL) occurs when τ_b is sufficient, at the sediment water interface, to initiate sediment motion (bedload transport) and resulting turbulent eddies induce vertical velocity components that exceed the particle fall velocity to resuspend sediment (Bagnold, 1966; Van Rijn, 1993). Here, τ_b is defined as a combination of the viscous stress (τ_v) and Reynolds stress ($\overline{\tau_R}$),

$$\tau_b = \tau_v + \overline{\tau_R} = \left(\rho\nu\frac{\partial U}{\partial z} - \rho\overline{u'w'}\right)\Big|_{z=0} \quad (1)$$

where the overbar denotes an averaged quantity and z is the vertical coordinate direction. The instantaneous horizontal velocity ($u = U+u'$) is Reynolds decomposed into mean (U) and turbulent (u') components, w' is the turbulent vertical velocity, ν is the kinematic viscosity and ρ is the fluid density.

Within the viscous sublayer, although $\overline{\tau_R} \to 0$, the bottom stress $\partial U/\partial z|_{z=0}$ is impractical to measure in the field. Theoretically, τ_b is constant throughout the boundary layer (constant stress layer), and a turbulent velocity scale can be introduced to represent the shearing strength (i.e., the friction velocity, u_*) at the sediment surface,

$$\tau_b = (\rho u_*^2)_{z=0} \quad (2)$$

To obtain u_* measured $u(z)$ profiles can be fit to the logarithmic law-of-the-wall,

$$u(z) = \frac{u_*}{\kappa} ln \frac{z}{z_0} \quad (3)$$

In Reynolds-averaged Navier-Stokes (RANS) models, applied at field-scale, these processes are often parameterized using the Quadratic Stress Law, which casts u_* in terms of the mean current velocity at a certain height above the sediment and a drag coefficient C_D (e.g., Boudreau and Jorgensen, 2001; Lorke, 2007),

$$u_*^2 = C_D U^2 \quad (4)$$

where the value of C_D depends on the height where the current velocity was measured, with 1 m being typical (Soulby et al., 1994; Lorke, 2007; Valipour et al., 2015a).

In natural aquatic systems, τ_b is not only generated from mean currents (Lick et al., 1994; Churchill et al., 2004), but also surface wave orbital velocities that impinge on the bottom (Lou et al., 2000; Hawley et al., 2004; Valipour et al., 2017). As a result, commonly applied parameterizations for τ_b, from field observations (e.g., Hawley et al., 1996; Hawley and Eadie, 2007) or in models (e.g., Lick et al., 1994; Lin et al. 2021b), are a summation of quadratic stress and surface wave-induced stress.

The concept that initiation of sediment resuspension depends on whether τ_b exceeds the theoretical time-averaged critical value (τ_{cr}) has long played a central role in sediment transport theory (Shields, 1936; Van Rijn, 1993; Soulsby and Whitehouse, 1997), and has been applied in sediment transport models (e.g., Warner et al., 2008). With the development of three-dimensional RANS models, this parameterization concept, and its modified versions, have also been used for field-scale numerical simulation of sediment resuspension and transport (e.g., Hu et al., 2009 [Delft3D]; Morales-Marin et al., 2018 [FVCOM-SED]; Niu et al., 2018 [FVCOM-SED]; Lin et al., 2021b [ELCOM-CAEDYM]). However, the algorithms applied in various

RANS models are not identical, with model-specific parameters requiring adjustment through calibration and validation against observed resuspension events.

While computationally suitable for inclusions in RANS equations models, the applicability of the Quadratic Stress Law to predict the occurrence of various types of resuspension events has been recently questioned (e.g., Boegman and Stastna, 2019). For example, in laboratory experiments (e.g., Boegman and Ivey, 2009; Aghsaee and Boegman, 2015) and field observations (e.g., Bourgault et al., 2014; Salim et al., 2018) sediment resuspension was associated with turbulent bursts, at times with sub-maximal τ_b, and when current velocities were below the critical value (e.g., Soulby et al., 1994; Yang et al., 2016; Salim et al., 2018). Thus, parameterization of τ_b based on temporal averaging of turbulent velocity fluctuations has been proposed

$$\tau_{TKE} = \rho C_t \overline{w'w'} \quad (5)$$

where C_t is a proportionality constant (Soulsby, 1983; Kim et al., 2000; Biron et al., 2004). Using single-point acoustic Doppler velocimeter (ADV) measurements of turbulent velocity fluctuations, (Bluteau et al., 2016) found τ_{TKE} to better predict sediment resuspension over the quadratic stress on the continental shelf, where internal waves shoaled. However, Zulberti et al. (2018) showed the quadratic stress (Eq. 4) to be as accurate as that from near-bed turbulence-based parameterizations (Eq. 5) in a similar flow, when measurements were close enough to the bottom.

It is evident that further reseaerch is required to enable better determination of τ_b from observed data and to better parameterize sediment resuspension in RANS models. The present enquiry-based study compares the different parameterizations to compute bottom stress from observations in central Lake Erie. The ability of RANS models to reproduce sedment resuspesnion events, using these parameterizations, is also assessed.

2. Method

2.1 Study area

Lake Erie (Fig. 1a) is a large (388 km long and 92 km wide) and shallow lake (19 m average and 64 m maximum depth) that can be divided into western, central, and eastern basins. The shallowness of the western and west-central basins makes them very susceptible to sediment resuspension by wind-induced surface waves (Sheng and Lick, 1979; Hawley and Eadie, 2007; Valipour et al., 2017). In the central and eastern basins of Lake Erie, a seasonal thermocline forms with near-inertial (~17 h) Poincaré waves being the dominant wind-induced motions during stratified period, in addition to the prominent (~14 h) surface seiche (e.g., Boegman et al., 2001; Rao et al., 2008; Valipour et al., 2015b). Although the topographic features of Lake Erie are complex and the sediment type and grain size vary among the basins, the most prevelent substrates in the lake include resuspendible silt, mud, and partially resuspendible glacial tills with grain sizes less than 63 μm (Haltuch et al., 2000).

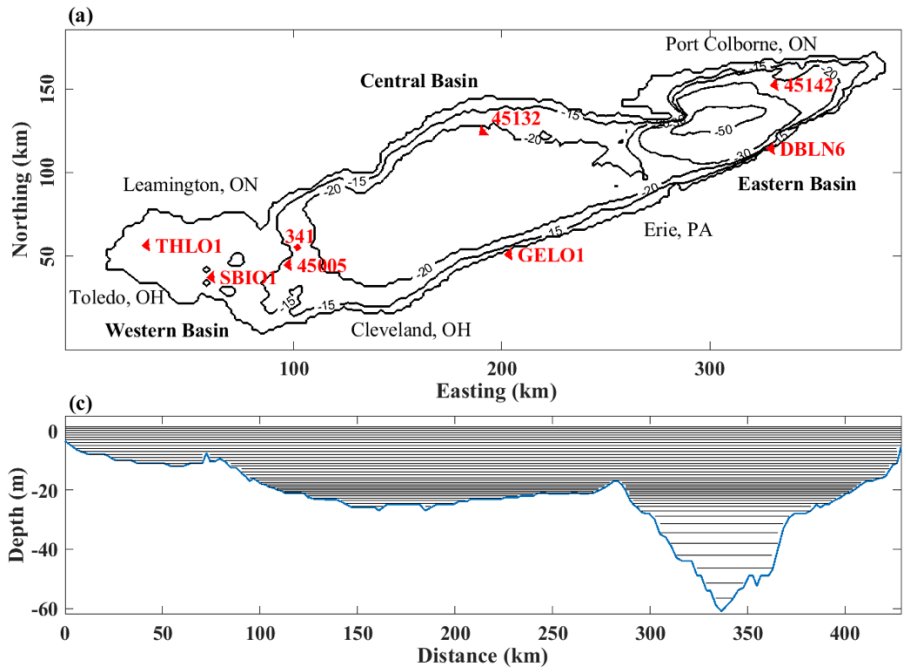

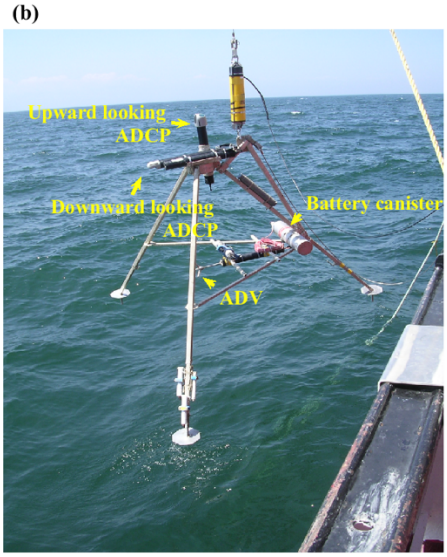

Fig. 1. (a) Map of Lake Erie showing the location of field observation (Sta. 341) and National Data Buoy Center (NDBC) wave buoy (45005). Negative numbers show the depth contours in meters. Red triangles are the sources of meteorological data used to drive the AEM3D and ELCOM models. (b) The tripod equipped with ADCPs, an ADV and RBR TR-1060s before deployment on the lakebed at Sta. 341 in 2008. (c) West-to-east curtain showing vertical grid (z-level) spacing in the models.

2.2 Field observations and critical shear stress

Field observations were conducted in west central Lake Erie (Sta. 341; Fig. 1a) during April-October of 2008-09, measuring water temperature, turbidity, total suspended solids (TSS), and both mean and turbulent current velocities near the lakebed (Supporting Information; Table S1). Water temperature was recorded at Sta. 341 using temperature loggers (TR-1060) on a taught mooring line. A 1.8 m tripod was deployed nearby the mooring (~30 m) on the lakebed, equipped with upward and downward looking Nortek Aquadopp acoustic Doppler current profiles (ADCPs; Fig. 1b). A Nortek Vector acoustic Doppler velocimeter (ADV) was on the tripod at 1 m above bottom (1 mab). Meteorological data and wave information was obtained from National Data Buoy Center (NDBC) Sta. 45005 located 15 km to the south-west of Sta. 341, from which surface wave orbital velocities (U_{orb}) and surface wave-induced stress (τ_w) were calculated (see 2.4.1, Eq. 6). Autoranging Seapoint turbidity and chlorophyll a (Chl-a) sensors logged to multi-parameter water quality sondes (RBR XR-620 and XR-420) located at 1.5 mab and 5 mab, respecitively.

From two superficial sediment samples collected at Sta. 341 on 26 August 2009, sediment particle diameters were measured d_{50} = 10μm (J. D. Ackerman, personal communication), and the bulk and granular densities were ρ_b = 1093 kg m^{-3} and ρ_s = 2150 kg m^{-3} (Valipour et al., 2017). The existing Shields diagram does not give a critical value for sediment finer than 40 μm. However, Valipour et al. (2017) observed high turbidity events near the bed of west-central Lake

Erie when the maximum instantaneous flow velocity (maximum value in each ADV burst; Table S1) $u_{max} > 0.25$ m s^{-1} , corresponding to $\tau_{max} = \rho C_D u_{max}^2 > 0.28$ Pa, where $C_D = 0.0045$; obtained by least-square fitting the burst averaged HR-ADCP velocity profiles to the law-of-the-wall (Valipour et al., 2015a). Their study also indicated that $u_{max} = 0.25$ m s^{-1} corresponded to a 5-min or burst-averaged flow velocity $u_{mean} = 0.1$ m s^{-1}, and consequently the critical value to trigger resuspension was $U_{cr} = 0.1$ m s^{-1}. Thus, we determined the time-averaged critical stress to be $\tau_{cr} = \rho C_D U_{cr}^2 = 0.045$ Pa in this study.

2.3 Identification of sediment resuspension events

Sediment resuspension events were qualitatively identified by an increase of turbidity and acoustic backscatter signal. Backscatter included the ADV backscatter amplitude (ADV-amp, unit [counts]) and in 2009 the HR-ADCP backscatter, corrected following (Lohrmann, 2001) for attenuation (ADCP echo, unit [dB]). The cross-correlation of these three indicators can be found in Valipour et al. (2017).

The turbidity sensor measurements include signals from suspended sediment and algal biomass, whereas the ADV and ADCP backscatter occur from sediment but not algae (Lohrmann, 2001). The *Chl-a* concentration recorded by the XR-420 in the spring of 2009 was used to exclude algal biomass events from the turbidity data. The ADCP echo profiles enabled identification of the particulate source, as originating from horizontal advection or local vertical resuspension.

To identify resuspension events within these data, we calculated the 7-day moving average and standard deviation of ADV-amp and turbidity. Resuspension was assumed when observations exceeded one standard deviation from the mean. By observations this approach distinguished resuspension events from background values.

2.4 Bottom shear stress parameterization based on observed data

Four parameterization methods for bottom stress were assesed in this study: 1) surface wave-induced stress (τ_w); 2) quadratic stress (τ_c); 3) log-law (τ_L); and 4) turbulent kinetic energy (τ_{TKE}). The total bottom stress, τ_b is be represented by $\tau_w + \tau_c$, τ_L, or τ_{TKE} .

2.4.1 Surface wave-induced stress

From wave theroy, τ_w is (Jonsson, 1966; Van Rijn, 1990),

$$\tau_w = 0.5\,\rho f_w U_{orb}^2 \quad (6)$$

where f_w is the wave friction coefficient,

$$f_w = \begin{cases} 2\left(\frac{a\times U_{orb}}{\nu}\right)^{-0.5} & \left(\frac{a\times U_{orb}}{\nu} < 10^4\right) \\ 0.09\left(\frac{a\times U_{orb}}{\nu}\right)^{-0.2} & \left(10^5 > \frac{a\times U_{orb}}{\nu} > 10^4\right) \\ \exp\left[-6 + 5.2\left(\frac{a}{k_s}\right)^{-0.19}\right] & \left(\frac{a\times U_{orb}}{\nu} > 10^5\right) \end{cases} \quad (7)$$

U_{orb} and a are the maximum orbital velocity (m s^{-1}) and the maximum bottom amplitude (m), respectively, given by linear wave theory

$$U_{orb} = \frac{\pi H_s}{T_s sinh(\frac{2\pi h}{L})} \quad (8)$$

$$a = \frac{H_s}{2sinh(\frac{2\pi h}{L})} \quad (9)$$

Here, h and H_s are the water depth (m) and wave height (m), T_s is the wave period (s), and L is the wavelength (m). These parameters were estimated from wind speed, fetch and water depth (Barua, 2005; Supplimentary material Table S1).

2.4.2 Quadratic stress

The Quadratic Stress Law combines (2) and (4) to relat stress (τ_c) to the mean current velocity,

$$\tau_c = \rho u_*^2 = \rho C_D U^2 \quad (10)$$

where $U = \sqrt{{U_x}^2 + {U_y}^2}$ is the burst-averaged mean horizontal current velocity 1 mab from the ADV. Here, U_x and U_y are the 5-min average current velocities in the east-west and north-south directions, which filters surface wave information.

2.4.3 Log-law method

In the log-law, a balance is assumed to exist between shear production and energy dissipation in the log layer. Under this premis, u_* can be derived from fitting observed mean velocity profiles to Eq. 3 (e.g., Valipour et al 2015a; Jabbari et al., 2021) or the rate of dissipation of turbulent kinetic energy (TKE) ε,

$$\tau_L = \rho u_*^2 = \rho(\varepsilon \kappa z)^{\frac{2}{3}} \quad (11)$$

where $\kappa = 0.4$ is the von Karman constant. For the log layer, there exists an inertial subrange where energy cascades from energy-containing eddies to energy-dissipating scales; the spectrum showing the inerital dissipation range has the Kolmogorov -5/3 form

$$\Phi_{ii}(k) = \alpha_i \varepsilon^{\frac{2}{3}} k^{-\frac{5}{3}} \quad (12)$$

where $\Phi_{ii}(k)$ is spectral density of ith velocity component at wavenumber k; in locally isotopic turbulence, α_i are one-dimensional Kolmogorov constants (Pope, 2000; Kim, et al., 2000). Near the lakebed, vertical velocities are less contaminated by mean currents than horizontal velocities (Jabbari et al., 2015), and the vertical turbulent velocity ($w' = w - \overline{w}$; w is the instantaneous vertical velocity, where the overbars denote 5-min averaging) is more likely to represent turbulent eddies. Thus, ε was obtained by fitting the energy spectrum of w' at a height z (1 mab) to the theoretical form within the inertial sub-range (see Supporting Information; Fig. S1), denoted ε_{ID}. We adopted α_i = 0.65 (i= 3 since we only considered vertical direction).

231 Both τ_c and τ_L assume the mean current velocity profile is logarithmic and the flow is
232 steady and unidirectional, but τ_c filters sub-grid-scale (turbulent and wave orbital velocities)
233 fluctuations, while τ_L (from Eq. 11, but not Eq. 3) retains turbulent information, including that
234 from wave orbitals.

235 *2.4.4 TKE method*

236 We applied a modified TKE method (Eq. 5) following Kim et al. (2000), Biron et al. (2004)
237 and Bluteau et al. (2016). The average ratio of τ_b to TKE is constant in the atmosphere (= 0.19;
238 (Stapleton and Huntley, 1995; Kim et al., 2000; Biron et al., 2004) and so by assuming linear
239 relationships between TKE and the vertical variance: $\overline{w'w'}$ = 0.59TKE (Pope, 2000), the constant
240 C_t was set to 0.32 (= 0.19 / 0.59). The modification was suggested (Kim et al., 2000), not only
241 because vertical velocity fluctuations have smaller instrument noise than horizontal velocity
242 fluctuations (Voulgaris and Trowbridge, 1998), but bursts of vertical velocity lift the bed
243 sediment more efficiently (Yuan et al., 2009; Aghsaee and Boegman, 2015). The TKE method is
244 expected to be better representation of τ_b in complex flow fields, where bursts of vertical
245 velocity are frequent or when the measurements are outside the logarithmic layer. At Sta. 341,
246 the logarithmic layer can extend to more than 10 m above the bed, but it also becomes limited by
247 baroclinic currents when stratification strengthens (Kim et al., 2000; Valipour et al., 2015a).
248 Thus, the independence of the TKE method from the logarithmic layer is expected to improve
249 accuracy in comparison to the other bottom stress parameterization.

250 **2.5 Flow interference**

251 The turbulence measurements were evaluated to identify if ε_{ID} or w'were contaminated by
252 vortex shedding from the mooring (Fig. 1b). The orientation of the ADV and locations of the
253 battery canister were different in 2008 versus 2009, allowing for varying directions associated

with flow interference. In 2008 (Fig. 1b), the main interference came from the external ADV battery canister; whereas, in 2009, the tripod frame was the source of interference (Valipour et al., 2015a). To identify interference, we correlated ε_{ID} to the third-power of the mean flow velocity at 1m above bottom (U_{1m}^3) (Supporting Information; Fig. S2; McGinnis et al., 2014; Jabbari et al. 2021). The ratio between predicted $\varepsilon_{p,1m}$ and observed ε_{ID} gave the flow directions contaminated with interference (Fig. S2d-f). The largest deviations, in 2008, was from a broad angle consistent with the location of the battery canister (Fig. S2d). In 2009, the largest deviation came from three narrow angles, indicating the tripod arms (Fig. S2e, f). The data contaminated with intererence were removed, leading to gaps in the τ_L and τ_{TKE} time-series.

2.6 Bottom shear stress parameterization in RANS models

We applied two coupled hydrodynamic and water quality RANS models ELCOM-CAEDYM (hereafter, ELCD) and AEM3D-iWaterQuality (hereafter AEM3D). The models are distributed by Hydronumerics (www.hydronumerics.com.au) and differ primarily in AEM3D being a new parallel version of ELCD, with reorganized biogeochemical algorithms. The models solve the unsteady RANS equations for incompressible flow, on a z-level finite difference grid, using Boussinesq and hydrostatic approximations (Hodges et al., 2000). A mixed layer approach is employed for turbulent closure, based on a TKE budget, with modeled dissipation (ε_m) available as a model output (e.g., Spigel et al., 1986). Model hydrodynamics (thermal structure, currents, internal wave dynamics, mixing rates, and sediment resuspension) have been well validated for Lake Erie (e.g., León et al., 2005; Liu et al., 2014; Valipour et al., 2015b; Bouffard et al., 2014; Lin et al., 2021a, b) using the same setup, and are not reported in detail herein. The water quality modules both predict resuspension when $\tau_b > \tau_{cr}$, where τ_b is the summation of surface wave-induced ($\tau_{w,m}$) and current-induced stresses ($\tau_{c,m}$); however, the algorithms for predicting these

stresses differ between the two models (see below).

2.6.1 Surface wave-induced stress

In ELCD, τ_w is from Eq. 6, where f_w is assumed to be for hydraulically rough flow, with k_s = 2.5 d_{50} and d_{50} is the median sediment grain size. In AEM3D, τ_w is related to a user-defined bottom drag coefficient C_D,

$$\tau_{w,m} = \rho_w C_D U_{orb}^2 \quad (13)$$

The calculation of wave properties, including wave orbital velocities can be found in Supporting Information (Table S2).

2.6.2 Quadratic stress

Both AEM3D and ELCD predict τ_c according to quadratic stress law. In ELCD,

$$\tau_{c,m} = \rho_w \frac{f_c U_{bot}^2}{8} \quad (14)$$

where $f_c = \frac{0.24}{[log(\frac{12\,\Delta z_{bot}}{k_s^\star})]^2}$ is the friction coefficient for hydraulically rough flow (van Rijn, 1993). In AEM3D,

$$\tau_{c,m} = \rho_w C_D U_{bot}^2 \quad (15)$$

where U_{bot} is the RANS modeled current speed in the bottom layer. Rather than relying on d_{50} for resuspension, through f_c, which also impacts particle settling, AEM3D allows users to apply a specified C_D. In the present application, we applied both *in situ* measured C_D = 0.0045 (Valipour et al., 2015a) and the canonical C_D = 0.0024 (Soulby et al., 1994) for mud/sand/gravel.

2.6.3 Log-law method

Both ELCD and AEM3D employ a TKE balance in their mixed layer closure scheme, which models dissipation (Hodges et al., 2000; Spigel et al., 1986)

$$\varepsilon_m = \frac{1}{2} C_\varepsilon \Delta t \left(\frac{TKE}{\Delta z}\right)^{\frac{3}{2}} \quad (16)$$

where the dissipation coefficient $C_\varepsilon = 1.15$, Δt is the timestep, Δz is vertical layer size, and *TKE* is the available mixing energy, which is the summation of wind stirring energy production, shear production between layers, and buoyancy production. Because Eqs. 14 and 16 are filtered in a RANS scheme, it would be informative to compare Eq. 11 using modeled grid-cell averaged dissipation (ε_m, which is also filtered) to that from the observed dissipation via inertial fitting (ε_{ID}).

2.6.4 TKE method

Reynolds-averaging filters sub-grid-scale turbulent fluctuations, providing only the mean flow. This makes it unrealistic to resolve turbulent vertical velocities and apply the TKE method (Eq. 5) to parameterize τ_b within a RANS model.

2.7 Model setup

ELCD and AEM3D were configured as in the validated ELCOM model applied by Liu et al. (2014), including meteorological forcing, inflows, outflows, and a 2 × 2 km horizontal grid with 45 vertical layers. A finer 0.5 m grid was set near the surface, through the thermocline and thin central basin hypolimnion, and coarser 5 m grid was set in the deep (~65 m) eastern basin (Fig. 1c); at Sta. 341, this gave a 0.75 m bottom layer to capture the thin bottom boundary layer. Validation of bottom mean currents and orbital wave velocities can be found below, in the Supporting Information (Fig. S3, 4) and the literature (e. g., León et al., 2005; Liu et al., 2014; Valipour et al., 2015b).

Spatial variability of meteorological conditions across the lake was applied using 6 surface zones with uniform meteorological forcing in the western, central (further subdivided into 4 zones), and eastern basins. The sources of meteorological data (Fig. 1a) included (1) Environment and Climate Change Canada (ECCC) lake buoy data (central basin, Port Stanley

45132; eastern basin, Port Colborne 45142), (2) US National Data Buoy Center (NDBC) buoys (western basin, station 45005), (3) Great Lakes Environmental Research Laboratory (GLERL) land stations (station THLO1), (4) US NDBC land stations (station SBIO1, GELO1, DBLN6). There were five inflows, including the Detroit, Maumee, Grand (Ontario), Sandusky and Cuyahoga Rivers, and only one outflow, the Niagara River (León et al., 2011). River water temperatures were taken as 3-day running averages of the air observed temperature. We initialized the model using observed water temperature profiles throughout the lake from a spring-summer survey (ECCC); whereas the initial velocity field was quiescent ('cold' start). Spin-up of this shallow wind driven system should be within a 17 h inertial period (Valipour et al., 2015b). In the 2008 model run, the observed TSS concentrations were specified from river loading (León et al., 2011) and pumped water samples collected at multiple stations were used as validation data and initial conditions (Bouffard et al., 2013). The models were run for 100 days in 2008 (days 203-303), and 157 days in 2009 (days 118-275), with a 5 min timestep, to satisfy the Courant-Friedrichs-Levy condition.

Sediments in the models were separated into three classes: river loads (SS_R, d_{50} = 3 μm; (Fukuda and Lick, 1980) and lakebed (SS_{B1}, d_{50} = 1 μm; SS_{B2}, d_{50} = 10 μm; Lick et al., 1994). SS_{B1} represented clay-like superficial (nepheloid) sediments (Lick et al., 1994), whereas SS_{B2} represented the silt-like sediments below (Hawley and Eadie, 2007; Valipour et al., 2017). The lakebed sediment classes were proportioned at 20% (clay) and 75% (silt), according to observations from the PONAR grabs (J. D. Ackerman, personal communication).

Results from ELCD and AEM3D were quantitively compared to the observation-based bottom stress parameterizations using the percent bias (P_{bias}), Pearson correlation coefficient (R), and the root-mean-square error ($RMSE$).

3. Results

3.1 Prediction of resuspension from observed τ_b

In the spring and summer, settling of algae (Paerl et al., 2011; Modis, NOAA Coastwatch-Great Lakes) contributed to some turbidity peaks consistent with high fluorescence (*Chl-a*) during the first deployment period (days 119-195) of 2009. We followed Valipour et al. (2017), who used the Medium Resolution Imaging Spectrometer (MERIS) to separate turbidity peaks due to resuspension from those due to high algal biomass (Sta. 341, days 226, 236, 245; Fig. 4b). We then identified twenty-three sediment resuspension events (Fig. 2-4; R1-23) from turbidity, ADV-amp and ADCP echo data. All three indicators showed resuspension during several especially intense events (R1, 3, 4, 7, 9, 12, 13, 21-23).

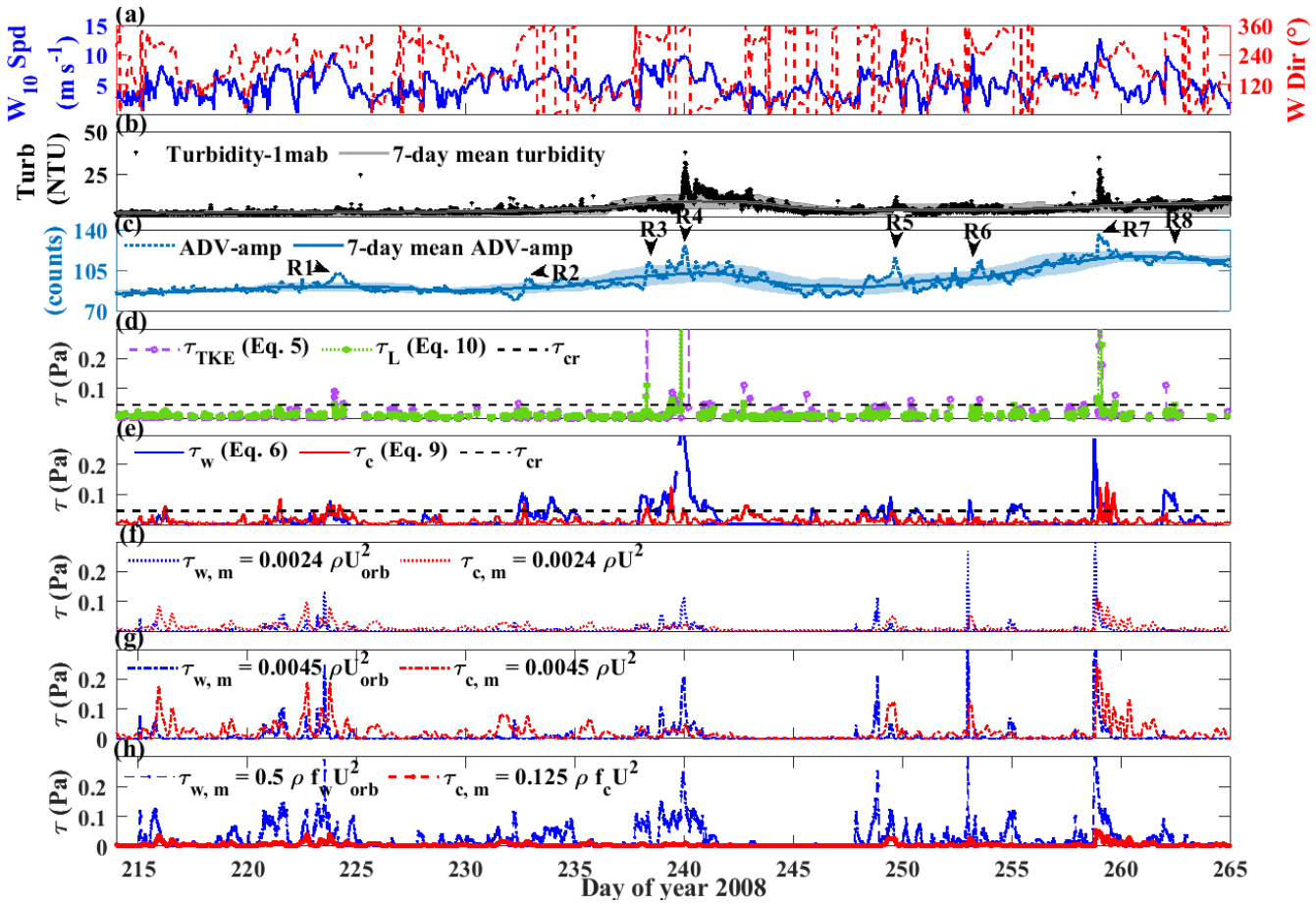

Fig. 2. Time-series at Sta. 341 for 2008 (a) wind speed (blue line; left y-axis) and direction (red dashed line; right y-

axis) at 10 m above water surface, (b) turbidity at 1.5 mab from XR-620 (black stars) and its 7-day moving mean (grey line) and 7-day standard deviation (grey shading), (c) ADV-amp at 1 mab (blue dots) and its 7-day moving mean (blue line) and 7-day standard deviation (blue shading), (d) τ_L (purple dash-dot line, Eq. 10), τ_{TKE} (green dash-dot line, Eq. 5) and critical value for resuspension (τ_{cr}=0.045 Pa; black dashed line), (e) τ_w (blue line, Eq. 6), τ_c (red line, Eq. 9) and τ_{cr}, (f-h) Modeled $\tau_{c,m}$ and $\tau_{w,m}$ based on varying C_D and algorithms.

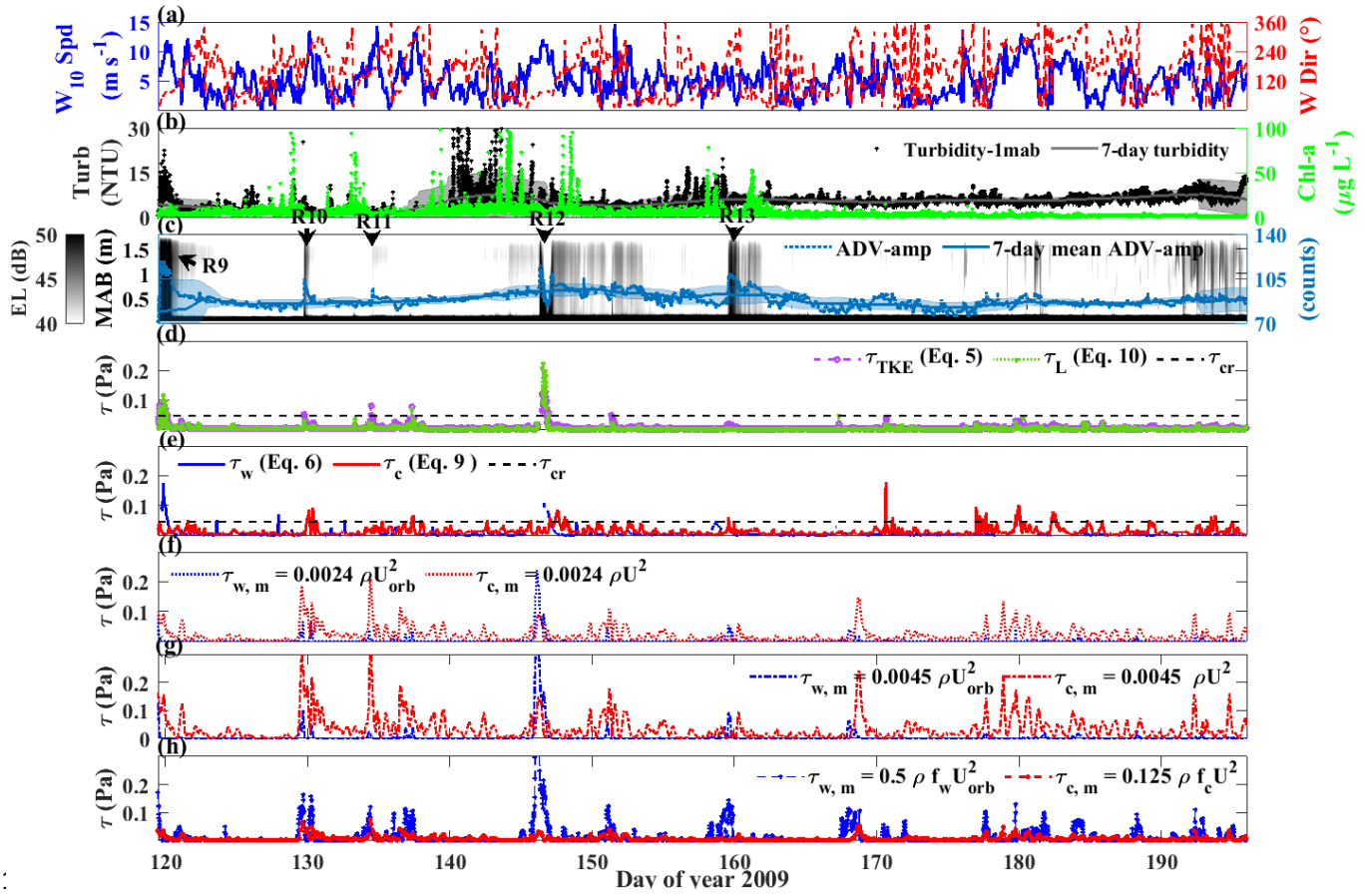

Fig. 3. Time-series at Sta. 341 for first deployment in 2009 (a) wind speed (blue line; left y-axis) and direction (red dashed line; right y-axis) at 10 m above water surface, (b) turbidity at 1.5 mab from XR-620 (black stars) and its 7-day moving mean (grey line) and standard deviation (grey shading) (left y-axis). Green stars are *Chl-a* concentration at 5 mab from XR-420 (right y-axis), (c) ADV-amp at 1 mab (blue dots) and its 7-day moving mean (blue line) and standard deviation (blue shading). Color bar shows the ADCP echo level, (d) τ_L (purple dash-dot line, Eq. 10), τ_{TKE} (green dash-dot line, Eq. 5) and τ_{cr} (black dashed line), (e) τ_w (blue line, Eq. 6), τ_c (red line, Eq. 9) and τ_{cr}, (f-g) Modeled $\tau_{c,m}$ and $\tau_{w,m}$ based on the algorithms in AEM3D with varying C_D (h) Modeled $\tau_{c,m}$ and $\tau_{w,m}$ based on the algorithms in ELCD.

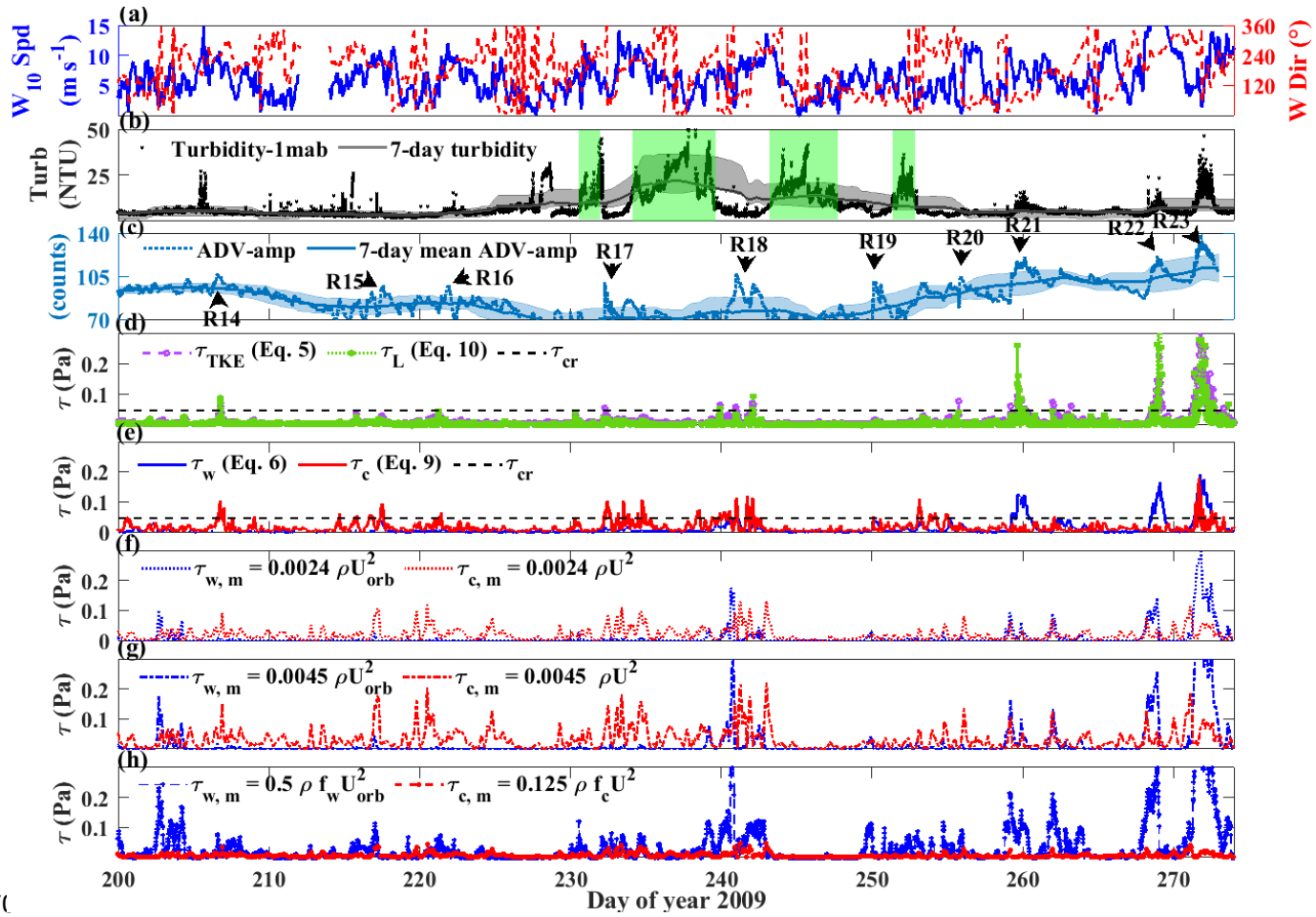

Fig. 4. Time-series at Sta. 341 for second deployment in 2009 (a) wind speed (blue line; left y-axis) and direction (red dashed line; right y-axis) at 10 m above water surface, (b) turbidity at 1.5 mab from XR-620 (black stars) and its 7-day moving mean (grey line) and standard deviation (grey shading), and green shading indicates the high turbidity from algae (Paerl et al., 2011), (c) ADV-amp at 1 mab (blue dots) and its 7-day moving mean (blue line) and standard deviation (blue shading), (d) τ_L (purple dash-dot line, Eq. 10), τ_{TKE} (green dash-dot line, Eq. 5) and τ_{cr} (black dashed line), (e) τ_w (blue line, Eq. 6), τ_c (red line, Eq. 9) and τ_{cr}, (f-g) Modeled $\tau_{c,m}$ and $\tau_{w,m}$ based on the algorithms in AEM3D with varying C_D (h) Modeled $\tau_{c,m}$ and $\tau_{w,m}$ based on the algorithms in ELCD.

The four parameterizations (Eq. 5, 6, 9, and 10) were applied to compute τ_b from the observed data and compared with τ_{cr} to predict the occurrence of resuspension events. During intensive resuspension events, $\tau_b = \tau_w + \tau_c$, τ_L, τ_{TKE} were qualitatively consistent, with spikes of different magnitudes (Fig. 2b-c, 3b-c, 4b-c; R1, 3, 4, 7, 9, 12, 14, 18, and 21-23).

Strong wind events created significantly increased τ_w, leading to surface wave-dominated resuspension events (e.g., R21 and R22; Fig. 5). During these events, high wind speeds (> 10 m

384 s^{-1}) were observed (see also Hawley and Eadie 2007). Given that wave orbitals penetrating to
385 the lakebed can form turbulent eddies, τ_L and τ_{TKE} often showed remarkable increases (> 0.2 Pa)
386 during surface wave-dominated resuspension.

387 Bottom current-dominated resuspension events were also observed (e.g., R14-17; Fig. 6)
388 with increased τ_c exceeding τ_{cr}. Both τ_L and τ_{TKE} were elevated (>0.045 Pa), indicating the
389 turbulent eddies formed due to bottom friction. Compared to surface wave-dominated
390 resuspension, R14–17 exhibited a more gradual increase in τ_L and τ_{TKE} (< 0.1 Pa), indicating
391 bottom currents were less efficient in triggering turbulent bursts compared to wave orbitals.

392 Most resuspension events were not induced by a single mechanism but resulted from
393 combined effects of surface waves and mean currents. Storm-induced mean currents have been
394 observed after strong wind events in Lake Erie (Lick et al., 1994; Beletsky et al., 1999; Hawley
395 and Eadie, 2007), leading to increased τ_c and generating resuspension (e.g., R1-5, 7, 9, 10, 12,
396 18, 19, 20, 23). However, τ_w or τ_c acting in isolation did not always reproduce the exact timing
397 of strong resuspension, rather τ_L and τ_{TKE} corresponded with peaks of ADV-amp and turbidity
398 more accurately (R7, R10, and R12; Fig. 7). This was in agreement with oceanic (Bluteau et al.,
399 2016) and laboratory (Aghsaee and Boegman, 2015) data, showing strong bottom drag to drive
400 bedload tranport, with turbulent bursts required to lift sediment into the water column. For
401 example, during day 146 in 2009 (R12) wind-driven surface wave orbitals impinged on the
402 lakebed, generating turbulence (τ_w ~ 0.1 Pa, τ_L and τ_{TKE} ~ 0.2 Pa; Fig. 7) and trigging
403 significant peaks in ADV-amp ADCP echo level, and turbidity. This was followed by barotropic
404 currents from basin-scale seiche events that formed as the wind subsided (Beletsky et al., 1999;
405 Valipour et al., 2015b) and generated $\tau_c > \tau_{cr}$ on day 147, leading to another peak in these three
406 resuspension indicaters.

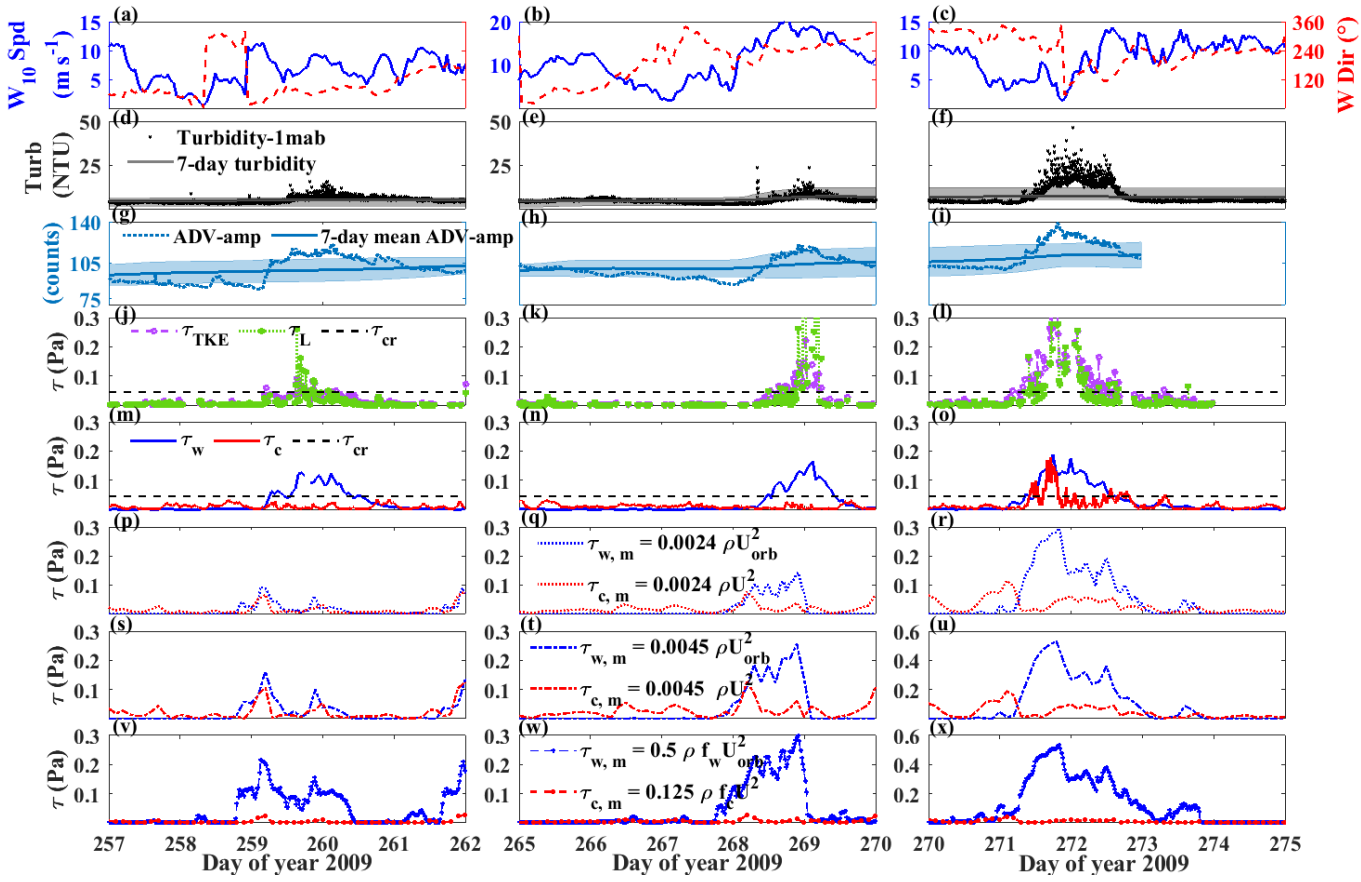

Fig. 5 Details of resuspension events R21-23 in Fig. 4. Time-series at Sta. 341 of (a-c) wind speed (blue lines; left y-axis) and direction (red dashed lines; right y-axis) at 10 m above water surface, (b-f) turbidity at 1.5 mab from XR-620 (black stars) and its 7-day moving mean (grey line) and standard deviation (grey shading), (g-i) ADV-amp at 1 mab (right y-axis), and its 7-day moving mean (blue line) and standard deviation (blue shading), (j-l) show τ_{TKE} (purple dash-dot line, Eq. 5) and τ_L (green dash-dot line, Eq. 10) based on turbulent velocity from ADV, and *in situ* critical value for resuspension τ_{cr} = 0.045 Pa, (m-o) τ_w (blue line, Eq. 6) based NDBC station 45005, τ_c (red line, Eq. 9) based on mean current velocity from ADV, and τ_{cr} (black dashed line), (p-r) AEM3D output $\tau_{w,m}$ (blue dotted line) and $\tau_{c,m}$ (red dotted line) used C_D = 0.0024, (s-u) AEM3D output $\tau_{w,m}$ (blue dashed line) and $\tau_{c,m}$ (red dashed line) used C_D = 0.0045; and (v-x) are ELCD output $\tau_{w,m}$ (blue dashed line) and $\tau_{c,m}$ (red dashed line).

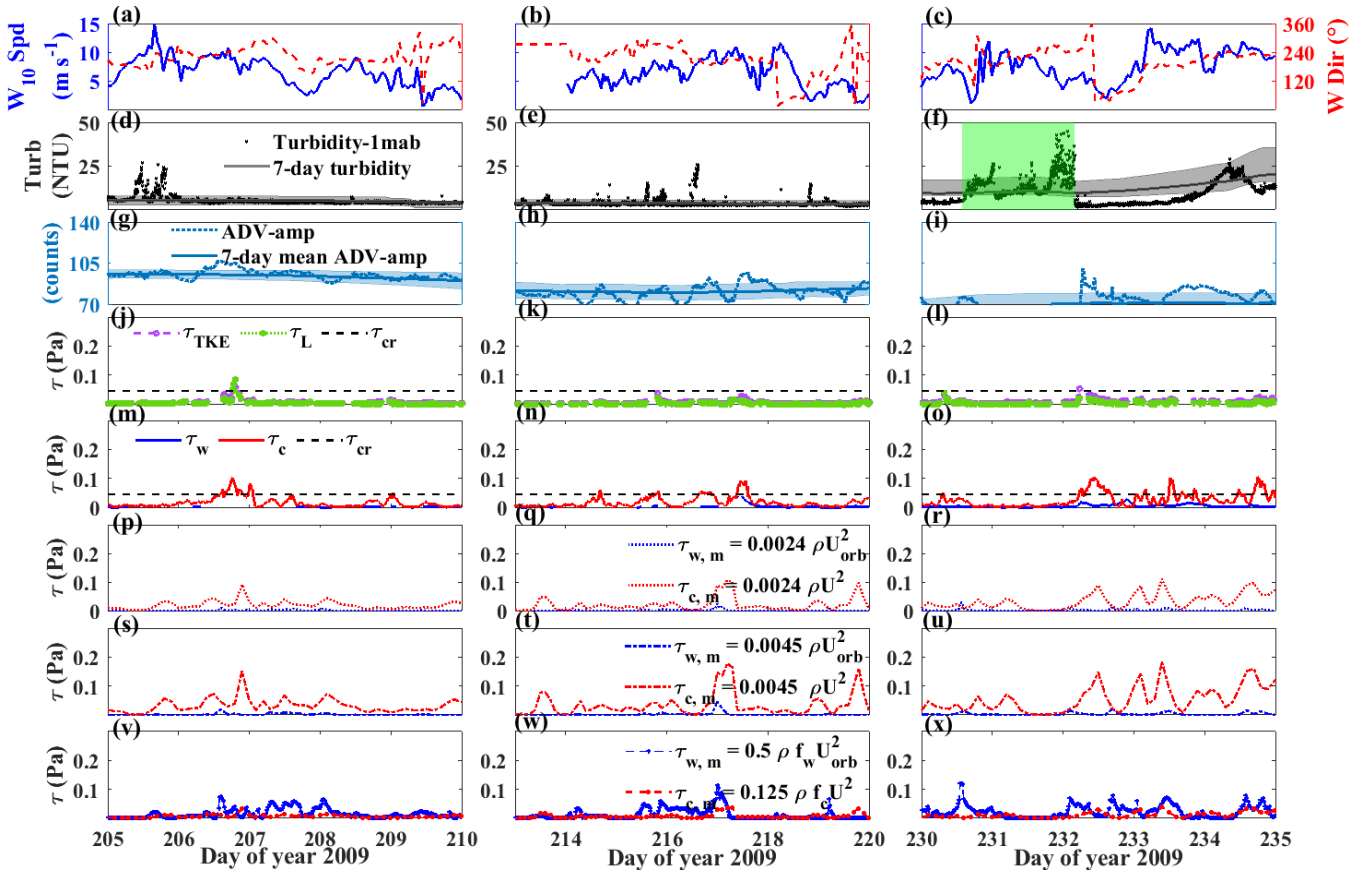

Fig. 6 Details of resuspension events R14, 15, 17 in Fig. 3. Time-series at Sta. 341 of (a-c) wind speed (blue lines; left y-axis) and direction (red dashed lines; right y-axis) at 10 m above water surface, (b-f) turbidity at 1.5 mab from XR-620 (black stars) and its 7-day moving mean (grey line) and standard deviation (grey shading), green shading indicates the high turbidity from algae (Paerl et al., 2011), (g-i) ADV-amp at 1 mab (right y-axis), and its 7-day moving mean (blue line) and standard deviation (blue shading), (j-l) show τ_{TKE} (purple dash-dot line, Eq. 5) and τ_L (green dash-dot line, Eq. 10) based on turbulent velocity from ADV, and *in situ* critical value for resuspension τ_{cr} = 0.045 Pa, (m-o) τ_w (blue line, Eq. 6) based NDBC station 45005, τ_c (red line, Eq. 9) based on mean current velocity from ADV, and τ_{cr} (black dashed line), (p-r) AEM3D output $\tau_{w,m}$ (blue dotted line) and $\tau_{c,m}$ (red dotted line) used C_D = 0.0024; (s-u) AEM3D output $\tau_{w,m}$ (blue dashed line) and $\tau_{c,m}$ (red dashed line) used C_D = 0.0045, and (v-x) are ELCD output $\tau_{w,m}$ (blue dashed line) and $\tau_{c,m}$ (red dashed line).

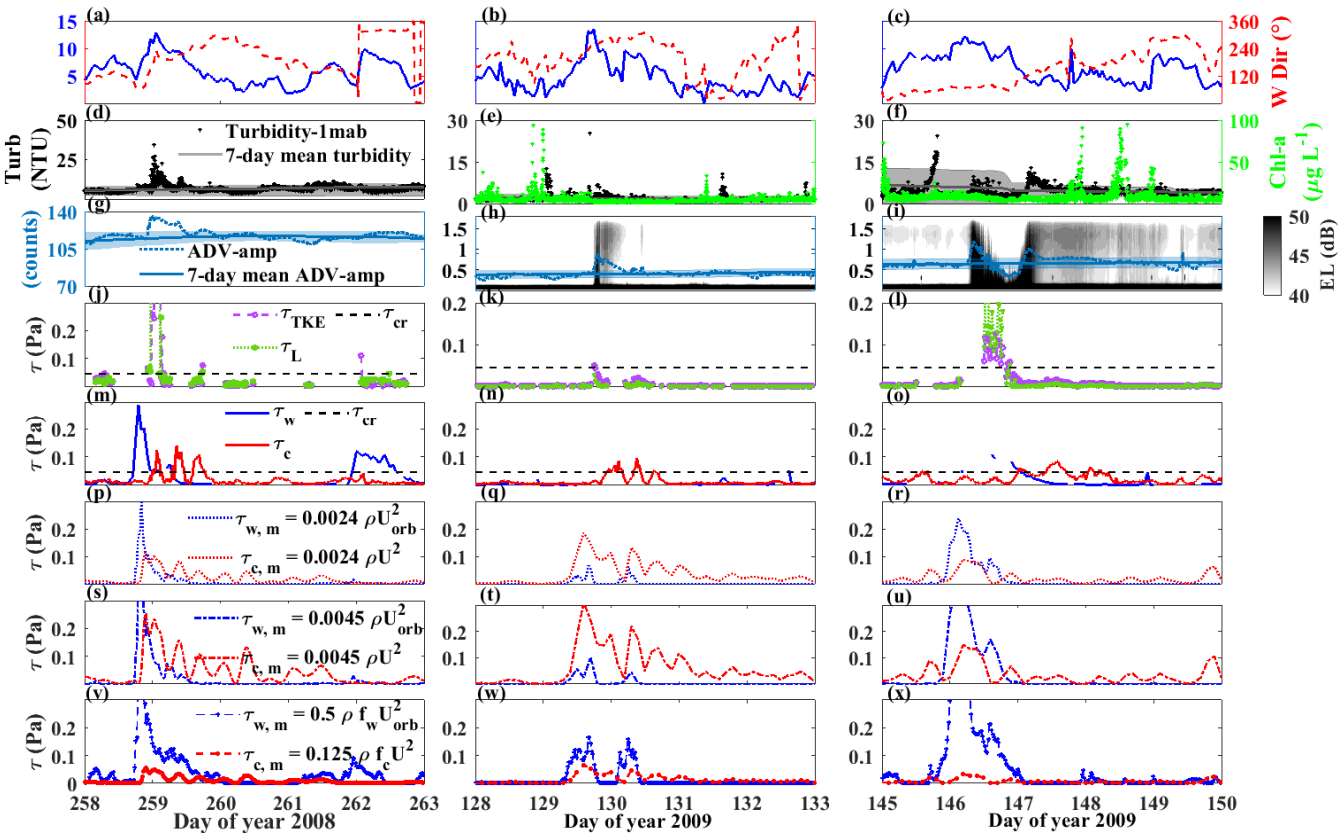

Fig. 7 Details of resuspension events R7, 10, 12 in Fig. 2, 3. Time-series at Sta. 341 of (a-c) wind speed (blue lines; left y-axis) and direction (red dashed lines; right y-axis) at 10 m above water surface, (b-f) turbidity at 1.5 mab from XR-620 (black stars) and its 7-day moving mean (grey line) and standard deviation (grey shading), and Chl-a concentration at 5 mab from XR-420 (right y-axis), (g-i) ADV-amp at 1 mab (right y-axis), its 7-day moving mean (blue line) and standard deviation (blue shading), and colorbar shows the ADCP echo level; (j-l) show τ_{TKE} (purple dash-dot line, Eq. 5) and τ_L (green dash-dot line, Eq. 10) based on turbulent velocity from ADV, and *in situ* critical value for resuspension (τ_{cr} = 0.045 Pa; black dashed line); (m-o) τ_w (blue line, Eq. 6) based NDBC station 45005, τ_c (red line, Eq. 9) based on mean current velocity from ADV, and τ_{cr} (black dashed line); (p-r) AEM3D output $\tau_{w,m}$ (blue dotted line) and $\tau_{c,m}$ (red dotted line) used C_D = 0.0024; (s-u) AEM3D output $\tau_{w,m}$ (blue dashed line) and $\tau_{c,m}$ (red dashed line) used C_D = 0.0045; and (v-x) are ELCD output $\tau_{w,m}$ (blue dashed line) and $\tau_{c,m}$ (red dashed line).

We have investigated the ability to parameterize resuspension by wave-orbital and seiche-induced mean currents; however, $\tau_b = \tau_c + \tau_w$ is not expected to be able to parameterize resuspension resulting from near-bed turbulent events forced by other processes (e.g., convection, Kelvin-Helmholtz billows). For example, Valipour et al. (2017) suggested that degeneration of Kelvin-Helmholtz billows could resuspend bottom material, when the induced turbulence

445 penetrated to the bed (see also Hawley et al., 2004; Austin, 2013). These events could only be
446 captured by τ_L and τ_{TKE}, because τ_c utilizes time-averaged mean currents that filter turbulence.
447 Here, we test the observational parameterizations for this type of event.
448 After a wind event on day 249 (Fig. 8), the thermocline, acting as a waveguide for high-
449 frequency internal waves (HFIW), impinged upon the lakebed (days 250-254). The HFIWs had
450 a period ~17 min (Valipour et al., 2017), which was close to the Brunt-Väisälä frequency and
451 much less than the ~17 hr inertial period; indicating they likely result from shear instability
452 across the thermocline (Bouffard et al., 2012; Boegman et al., 2003). During this 10-day event,
453 $\tau_b = \tau_c + \tau_w > \tau_{cr}$ on days 248-9 (Fig. 8e), corresponding to an increase of ADV-amp and
454 turbidity (R6). This was followd by spikes in τ_L and τ_{TKE} above τ_{cr} on days 252 and 253.5,
455 corresponding to peaks in ADV-amp and high turbidity (Fig. 8d). At these times, when τ_w and τ_c
456 were close to zero, HFIWs were carried on the near-bed thermocline (Fig. 8b); because the
457 peaks in τ_L and τ_{TKE} matched peaks in ADV-amp and turbidity, this suggested the mechanism
458 triggering near-bed high turbidity could be turbulent eddies generated by collapse of Kelvin-
459 Helmholtz billows as the HFIWs degenerate (Fig. 8c, d). Compared to resuspension induced by
460 τ_c or τ_w, the intensity of resuspension generated during HFIWs was lower. Both turbidity and
461 ADV-amp were elevated for several days, showing that turbulent eddies, generated when the
462 thermocline impinged on the lakebed, created an oscillatory nepheloid-type layer in the
463 hypolimnion. In this example, τ_L and τ_{TKE} provided a better estimate of sediment resuspension.
464 Overall, the observations spanning the summer of 2008 and spring-fall of 2009 revealed that
465 τ_L and τ_{TKE} showed peaks during resuspension triggered by surface wave orbitals, mean bottom
466 currents and HFIWs. The magnitude of the stress was relatively higher in magnitude during
467 resuspension involving a contribution from surface waves (e.g., R7, 12, 21-23; Fig. 5, 7) and

relatively lower in magnitude during resuspension from mean bottom currents or HFIWs (e.g., R10, 14-17; Fig. 6, 7). Moreover, $\tau_b = \tau_w + \tau_c > \tau_{cr}$ was able to predict all resuspension events induced by wave orbitals (R8, 21, 22), increased bottom currents (R13, 14-17) and a combination of these two mechanisms (R1-5, 7, 9, 10, 12, 18, 19, 20, 23).

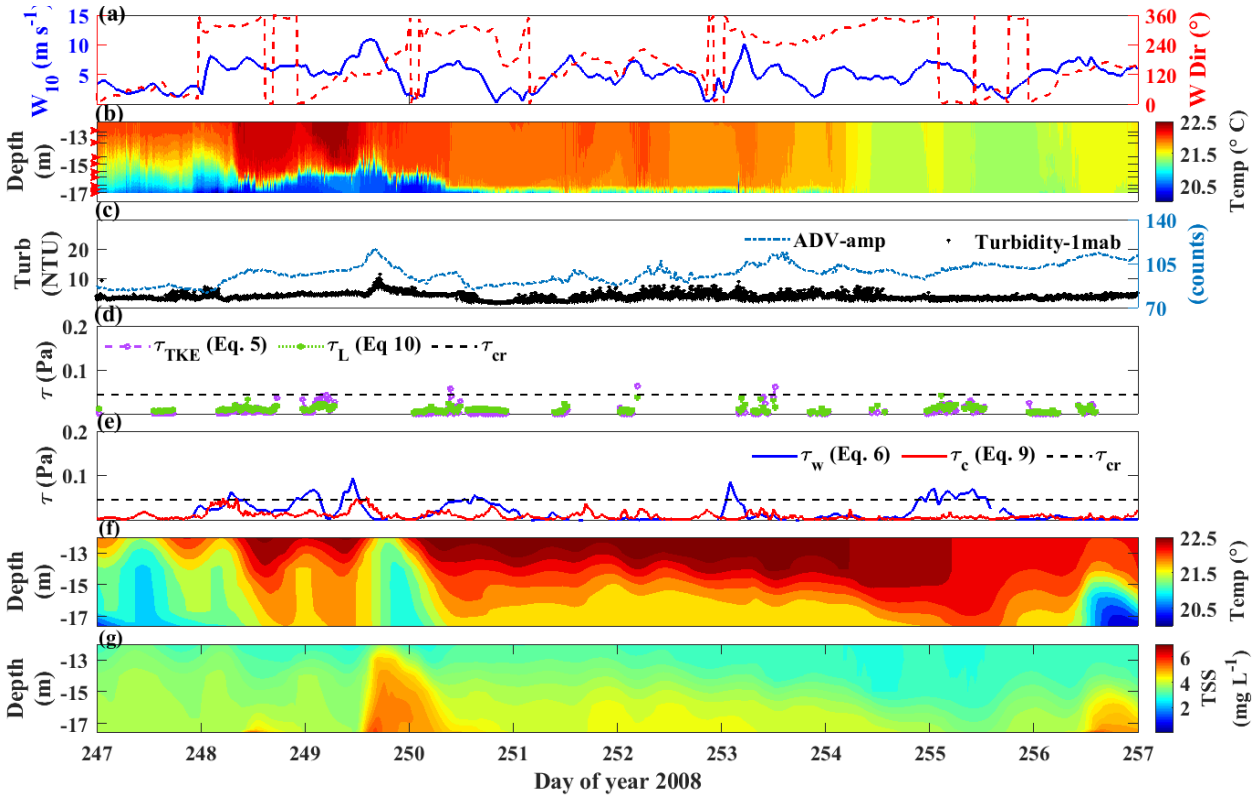

Fig. 8 Details of resuspension events R6 in Fig. 2. Time-series at Sta. 341 of 2008 (a) wind speed (left y-axis) and direction (right y-axis) at 10 m above water surface, (b) temperature contours from TR-1060 temperature loggers, red arrows show vertical locations of temperature loggers, (c) turbidity at 1.5 mab from XR-620 (left y-axis), and ADV-amp at 1 mab (right y-axis); (d) and (e) show τ_L (green dash-dot line, Eq. 10), τ_{TKE} (purple dash-dot line, Eq. 5), τ_w (blue line, Eq. 6), τ_c (red line, Eq. 9) based on observd data and τ_{cr} (black dashed line); (f) and (g) are ELCD output of temperature and TSS concentration at Sta. 341, respectively.

3.2 Prediction of resuspension from RANS modeled τ_b

Here, we compare the observed bottom stress, required for resuspension, against those simulated by the models. ELCD qualitatively captured the occurrence of strong resuspension events induced by both bottom currents and surface waves in 2008 and 2009 (Lin et al., 2021b)

(Supporting Information, Fig. S4, S5). However, as calibrated against the turbidity data, the threshold for sediment resuspension in ELCD (0.01- 0.025 Pa) was lower than the observed *in situ* time-averaged threshold (τ_{cr} = 0.045 Pa).

The present magnitude of $\tau_{c,m}$, parameterized based on the Reynold-averaged current speed (Eq. 14), was much less than the observed τ_c (Figs. 3-5 e, h). Because wave stresses were overestimated with ELCD ($\tau_{w,m} > \tau_w$; Figs. 3-5 e, h), having $\tau_{c,m} \ll \tau_{w,m}$ creates problems specifying τ_{cr} within the modelling framework. Unrealistic setting of τ_{cr}, to capture current-induced resuspension, will cause ELCD to respond excessively to surface wave forcing, and overestimate the contribution of surface waves to resuspension (e.g., R14 - R17; Fig. 2-4). Adjustment of $\tau_{c,m}$ within ELCD to resuspend at an appropriate τ_{cr}, by increasing bed roughness (k_s = 2.5 d_{50}; d_{50} is the median sediment grain size) in Eq. (14), is not possible because of the effect of d_{50} on particle settling (Lin et al., 2021b).

The modeled U_{orb} and U_{bot} are calculated with the same algorithms in both AEM3D and ELCD (Supporting Information, Fig. S4); therefore, both overestimated the peak current speeds (U_{bot} *RMSE* = 0.051 m s^{-1}). There were insufficient observed wave orbital velocity measurements to calculate U_{orb} error.

AEM3D avoids the particle settling issues in ELCD by directly employing C_D to parameterize both $\tau_{w,m}$ and $\tau_{c,m}$ (Eq. 13, 15). The AEM3D-modeled bottom current velocities are not sensitive to small variations of C_D (C. Dallimore, personal communication); therefore, adjustment of bottom drag focused on reproducing bottom stress, rather than bottom currents. Table 1 shows the comparison of parameterizations for $\tau_{w,m}$ and $\tau_{c,m}$ in AEM3D and ELCD. ELCD (Eq. 6) overestimated surface wave-induced stress (Fig 3-5 e, h), with *RMSE* = 0.052 Pa and P_{bias} = 57% (Table 1; $\tau_{w,m1}$). The error was less using the parameterization in AEM3D (Eq. 13), with *RMSE* = 0.031Pa and P_{bias} ~ 0 when C_D = 0.0024 (Fig. 2-4 e, f).

The parameterization of quadratic stress in ELCD (Table 1, $\tau_{c,m1}$) gave the lowest *RMSE*, but the P_{bias} = -46% showed the overall underestimation of the magnitude (Fig. 2-4 h). Given that ELCD and AEM3D overestimate current speed, particularly the peak values (Fig. S4), when applying the observed C_D = 0.0045 in Eq. 15 (Tabel 2, $\tau_{c,m2}$) the P_{bias} was highest (196%) amongst the three parameterizations. Thus, applying the canonical C_D = 0.0024 in Eq. 15 compensated for overestimation of current speed, reproducing an appropriate magnitude for the quadratic stress (Figs. 3-5 e, f). This gave *RMSE* = 0.025 Pa and the lowest P_{bias} (= 34%).

3.3 Turbulence-based parameterizations in RANS models

The inability of the models to resolve the sub-grid turbulence, may result in only a subset of resuspension events being simulated, and those resulting from mean shear-free boundary turbulence (Johnson and Cowen, 2020) being neglected (e.g., HFIW events). Thus, we applied Eq. 11, using the modeled ε_m (Eq. 16) to assess the possibility of employing a log-law based turbulence parameterization in a RANS sediment model. Here, the modeled/observed turbulence may result from mean shear-free processes (e.g., convection), but the resultant stress follows log-law scaling (Eq. 11). The computed $\tau_{L,m}$ was higher than the observed τ_L most of the times (Fig. 9) and the model was unable to capture peaks in observed τ_L. Table 1 shows the agreement between $\tau_{L,m}$ and τ_L is poor (R^2 = 0.05). To investigate why, ε_{ID} and ε_m were compared at selected periods (Supporting Information, Fig. S7), showing reasonable qualitative comparison, but frequent quantitative differences of more than an order of magnitude. This was not unexpected as the modeled dissipation output is the TKE remaining at the end of a timestep and, therefore, is useful as a diagnostic output for the individual components in the TKE parametrization (C. Dallimore, personal communication).

Table 1

Assessment of bottom stress parameterization in ELCD (denoted by m1) and AEM3D (denoted by m2, 3) models.

	Modeled $\tau_{w,m1}$	Modeled $\tau_{w,m2}$	Modeled $\tau_{w,m3}$	Modeled $\tau_{c,m1}$	Modeled $\tau_{c,m2}$	Modeled $\tau_{c,m3}$	Modeled $\tau_{L,m}$
RMSE	0.052 Pa	0.042 Pa	0.031 Pa	0.017 Pa	0.047 Pa	0.025 Pa	1.7 Pa
R^2	0.51	0.46	0.47	0.15	0.13	0.15	0.05
P_{bias}	57%	-27%	-2.2%	-46%	196%	34%	80%

$\tau_{w,m1} = 0.5\ \rho f_w U_{orb}^2$; $\tau_{w,m2} = 0.0045\ \rho U_{orb}^2$; $\tau_{w,m3} = 0.0024\ \rho U_{orb}^2$

$\tau_{c,m1} = 0.125\ \rho f_c U^2$; $\tau_{c,m2} = 0.0045\ \rho U^2$; $\tau_{c,m3} = 0.0024\ \rho U^2$

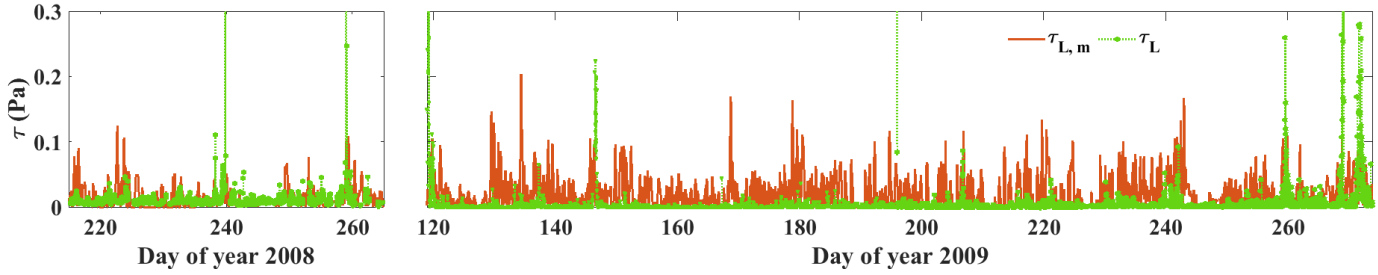

Fig. 9 Time-series at Sta. 341 of τ_L (Eq. 11) based on ε_m (Eq. 16, orange line) and ε_{ID} (green dash-dot line). Comparisons of observed and modelled turbulent dissipation are shown in Fig. S6.

3.4 Sediment resuspension hot spots

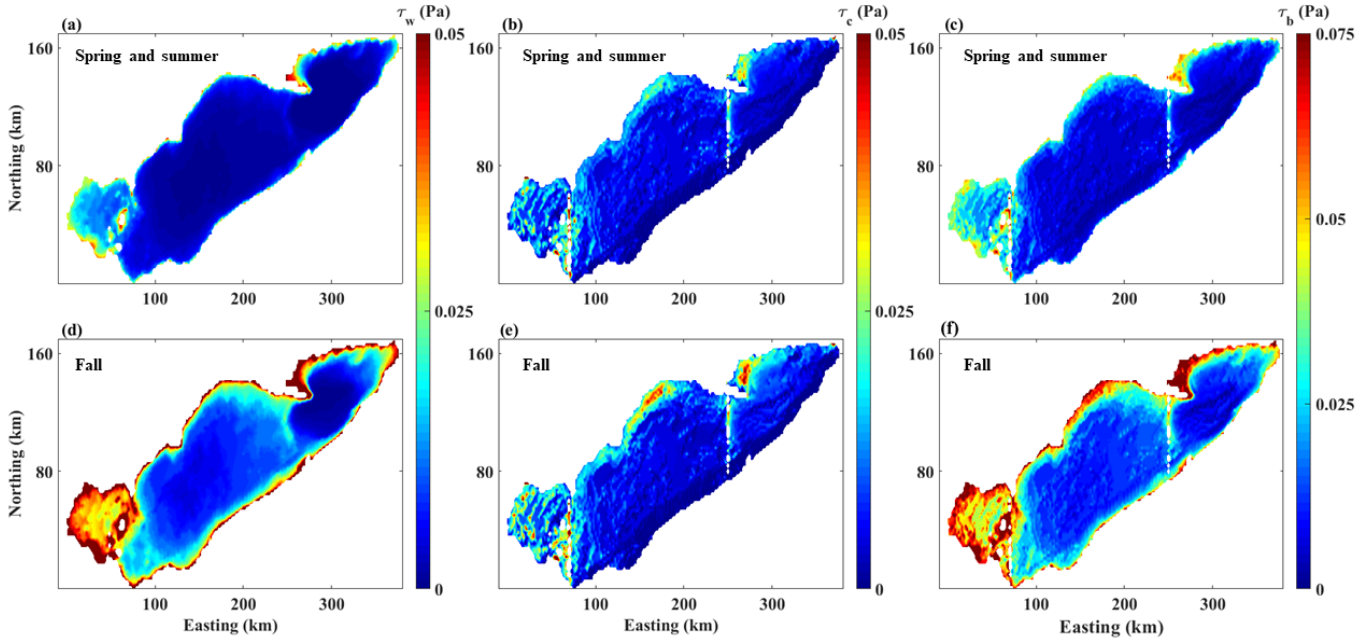

Fig. 10 Mean value of AEM3D modeled $\tau_{w,m}$, $\tau_{c,m}$, and τ_b (a-c) over spring and summer (days 203 – 245 of 2008 and days 119- 250 of 2009), and (d-f) over fall (days 245- 303 of 2008 and days 250 – 300 of 2009).

To visualize variation in bottom stress throughout the basin, AEM3D simulated $\tau_{w,m}$, $\tau_{c,m}$ and $\tau_b = \tau_{w,m} + \tau_{c,m}$ were computed for different seasons (Fig. 10) using the AEM3D parameterization based on Eqs. (13 and 15) with $C_D = 0.0024$. Resuspension hot spots were identified as sites where $\tau_b = \tau_{w,m} + \tau_{c,m}$ exceeded $\tau_{cr} = 0.045$ Pa . In general, both $\tau_{w,m}$ and $\tau_{c,m}$ increased in fall when storms are more prevalent on the lake.

The effect of surface wave orbitals decreased with increasing water depth, with the western basin and littoral zones having the highest $\tau_{w,m}$. The area of modeled surface wave-induced resuspension hot-spots increased from 80 km^2 before fall turn over to 2592 km^2 after fall turnover (Fig. 10a, d) due to the more frequent storms (Fig. 2-4 a). The current-induced resuspension hot-spots were often associated with bottom topography (e.g., the Point Pelee to Sandusky island chain and the Pennsylvania Ridge; Fig. 10b, e) and were otherwise sporadically distributed in the western basin and along the north shore of the central and eastern basins. The area of hot-spots increased from 84 km^2 before fall turnover to 168 km^2 after fall turnover (Fig. 10b, e). During the spring and summer, most of the current-induced resuspension was driven by wind-energized seiche events and baroclinic currents (e.g., Hawley, 2004; Rao et al., 2008; Valipour et al., 2017). Combining wave-induced and current-induced stresses, the total area of resuspension hot-spots was 1920 km^2 in spring and summer and 5196 km^2 in fall, being concentrated in the western basin, and the northern shoreline of the central and eastern basins (Fig. 10c, f).

4. Discussion

4.1 Comparison of algorithms in commonly applied hydrodynamic models

The AEM3D and ELCD bottom stress parameterizations are discussed with reference to the parameterizatons in other commonly-applied hydrodynamic models, specifically FVCOM-SED and Delft3D (Table 2).

Table 2

Parameterizations for τ_c in different sediment models. The equations in column 2 were solved using parameters characteristic to Lake Erie (column 4).

Method	τ_c equation		d_{50} (m)	τ_c (using parameters in Lake Erie)
In situ observation	$\rho^{*} C_D U^2$		10^{-5}	$4.5U^2 (C_D = 4.5 \times 10^{-3})$
FVCOM-SED	$\rho\ max\left[\frac{\kappa^2}{\ln(\frac{\Delta z_{bot}}{z_o{}^{\ddagger}})^2}, 0.0025\right] U_{bot}^2$		10^{-5}	$max[0.00082, 0.0025]\ \rho U^2 = 2.5U_{bot}^2$
Delft3D	2D flow	$\rho \frac{g}{(18\,[log_{10}(\frac{12h^{\#}}{30z_o{}^{\ddagger}})]^2} U_{bot}^2$ (White Colebrook)	10^{-5}	$0.64U_{bot}^2$
		$\rho \frac{g}{(\frac{\sqrt[6]{h^{\#}}}{n^{\dagger}})^2} U_{bot}^2$ (Manning)	10^{-5}	$3849 n^{\dagger 2} U_{bot}^2 = 0.23U_{bot}^2$
	3D flow	$\rho \frac{\kappa^2}{\ln(1+\frac{\Delta z_{bot}}{2z_o{}^{\ddagger}})^2} U_{bot}^2$	10^{-5}	$0.9U_{bot}^2$
ELCD	$\rho \frac{0.24}{[log(\frac{12\ \Delta z_{bot}}{k_s{}^{\star}})]^2} U_{bot}^2$		10^{-5}	$0.97U_{bot}^2$
AEM3D	$\rho C_D U_{bot}^2$		10^{-5}	$4.5U_{bot}^2$ (C_D= 0.0045) $2.4U_{bot}^2$ (C_D= 0.0024)

$\ast\ \rho$ Water density = 1000 kg m^{-3}

$*\ \Delta z_{bot} = 1$ m The thickness of the bottom layer in the models

$\#\ h = 16.5$ m The depth of model output current velocities

$\dagger\ n$ User-defind manning coefficient. Theoretically, $n = 0.045(2.5\ d_{50})^{1/6}$ (van Rijn, 1993).

$\ddagger\ z_o$ Roughness height of the lakebed (i.e., zero velocity level) [m]: $z_o = 0.083\ d_{50}$

$\star\ k_s$ bed roughness, $k_s = 30\ z_o$[m]. Several relations between k_s and bottom sediment grain size have been proposed, with one of the most widely used being: $k_s = 2.5\ d_{50}$.

ELCD, FVCOM-SED and Delft3D all use logarithmic scaling for C_D based on k_s or z_o, which are both associated with bed roughness (Table 2). In RANS models, the resolution of the bathymetry is insufficient to resolve bedforms, which are difficult to measure, and consequently sediment grain size is employed to calculate C_D (Table 2). As a result, C_D in these models will be smaller than *in situ* observations (0.0045), which account for the effects of bottom morphometry on drag. To adjust $\tau_{c,m}$ to become equivalent to the *in situ* τ_c, d_{50} (when involved into the calculation of τ_c; e.g., in ELCD or FVCOM-SED) should be set to 0.03 m, which is not realistic. To alleviate this issue, FVCOM-SED sets a minimum $C_D = 0.0025$ (close to the canonical value of 0.0024), bringing $\tau_{c,m}$ in FVCOM-SED closest to the observed values among these three models (Table 2; Morales-Marin et al., 2018; Niu et al., 2018). Similarly, Hu et al. (2009) applied the DELft3D 2D flow $\tau_{c,m}$ but set the Manning coefficient independently of d_{50} (Table 2), so the model could correctly reproduce sediment resuspension using a literature-based τ_{cr}. From Table 2, the difference in parameterizaitons is reduced to the constant in front of U_{bot}^2. Given that models tend to overestimated bottom current speed (Fig. S4), the constant not only embodies bottom drag, but also adjusts for errors in hydrodynamic model output. For examle, to parameterize resuspension with $U > U_{bot}$ we may use $2.4U_{bot}^2 \approx 4.5U^2$. This suggests the optimal C_D in the model can be computed from the observed value and ratio of observed to modelled velocities as $C_D^{model} = C_D^{obs.}(U^2/U_{bot}^2) = (4.5 \times 10^{-3})(2.4/4.5) = 2.4 \times 10^{-3}$.

The ELCD results in 2008 showed that (i.e., $\tau_{w,m}$) played a dominant role in the west central basin of Lake Erie during intense storm events (Valipour et al., 2017; Lin et al., 2021b). But Morales-Marin et al. (2018), who applied FVCOM-SED, modeled a much larger relative proportion of the lakebed to be potentially resuspended by currents during extreme wind events in an upland shallow lake in north Wales (UK). One explanation for this discrepancy is that

592 western Lake Erie has a longer fetch and so can develop stronger surface waves over its shallow
593 water depth. Another possible reason is the underestimation of the contribution from currents
594 because of the inappropriate algorithms in ELCD. Thus, by applying AEM3D with Eq. 15, the
595 magnitude of the modeled stress was closer to the observed value (Fig. 2-4 e, f, g), and the
596 relative contributions of from bottom currents were comparable to those from surface waves
597 during storms (e.g., R1, 13, 18; Fig. 2-4) in west central Lake Erie (Sta. 341). However, the
598 shallow Lake Erie morphology results in strong surface waves during intense storm events (e.g.,
599 R23; Fig. 4) dominating the overall resuspension.

600 From these comparisons, the core concept of the $\tau_{c,m}$ parameterization is determination of
601 the constant before U_{bot}^{2}. Thus, we summarized two ways to parameterize $\tau_{c,m}$ in RANS models.
602 The first is to apply an *in situ* or literature-based canonical C_D value, if available, to Eq. 15
603 (Soulby et al., 1994; Zulberti et al., 2018) and adjust C_D to account for inaccuracy in modelling
604 currents, especially the peak values (Fig. S4). The second option is parameterization like
605 FVCOM-SED, which chooses the maximum value between the logarithmic derived C_D and the
606 user-defined minimum C_D; this option requires knowledge of bed roughness z_o in the model.

607 **4.2 Parameterization based on near-bed turbulence**

608 The τ_{cr} defined by existing threshold models is most often determined by flume
609 experiments using mean current velocity profiles (Shields, 1936; Soulsby et al., 1997). However,
610 on larger scales and in more complex systems (e.g., shallow marine environments and large
611 lakes), the threshold could be reduced because of the enhanced intensity of intermittent turbulent
612 events (Salim et al., 2018; Yang et al., 2016), including resuspension from mean shear-free
613 turbulence (Johnson and Cowen, 2020). Therefore, parameterizing τ_b from time-averaged
614 current speeds is not always appropriate for modelling the bottom nephyloid layers in the

presence of trubulent bursting events (Bourgault et al., 2014; Aghsaee and Boegman, 2015), including the turbid hypolimnion beneath HFIWs in this study. In these cases, τ_{TKE} and $\tau_L$are more appropriate because both methods parameterize near-bed turbulence (Eq. 5, 11).

Existing RANS models are unable to resolve *w'*, and so parameterizations using TKE are unrealistic. Present algorithms for ε_m in RANS models (e.g., AEM3D) do not consider the energy flux path associated with surface wave generation and breaking (e.g., Spigel et al., 1986; Hodges et al., 2000), leading to overestimation of the energy flux entering the lake interior most of the time (Fig. S6). Fig. 9 shows that $\tau_{L,m}$ was smaller than the observed τ_L, only when bottom stresses were mainly from surface wave orbital velocities (R4, 7, 9, 12, 21-23). Therefore, complete replacement of the present parameterization (Eq. 10, 14) with $\tau_{L,m}$ is not suitable for shallow water systems with resuspension frequently triggered by surface waves. The development of turbulence-based parameterizations should be an avenue of future work, particularly for systems with intensive convective turbulence (Anderson et al., 1979; Johnson and Cowen 2020), where shear-driven models are inappropriate.

5. Conclusions

Multiple parameterization methods for bottom stress (τ_b), including (1) sum of surface wave stress and mean current (quadratic) stress ($\tau_b = \tau_w + \tau_c$; Eq. 6, 10); (2) log-law ($\tau_b = \tau_L$; Eq. 11); and (3) turbulent kinetic energy ($\tau_b = \tau_{TKE}$; Eq. 5), have been assessed, based on observed data and model output. For large and shallow waterbodies, bottom currents and surface wave orbitals were the two major processes driving bottom sediment resuspension and $\tau_b = \tau_w + \tau_c$ was sufficient to qualitatively predict resuspension. This model was readily calibrated for sediment resuspension simulations in field-scale RANS models. Sub-grid-scale hydrodynamics (HFIWs) also induced low-intensity resuspension events, when the seasonal

thermocline became close to the lakebed, and only τ_L and τ_{TKE} were able to capture the turbid bottom layer generated by these events.

This study assessed different parameterizations for $\tau_{w,m}$ and $\tau_{c,m}$ in the RANS models and the model parameterizations via Eq. 13 and 15 with canonical C_D showed lowest P_{bias} (34% and -2.2%, respectively) when compared to parameterizations based on observed data (Eq. 6, 10). In some commonly-applied hydrodynamic models, the parameterizations using logarithmic scaling for C_D based on bed roughness, could potentially lead to underestimation of bottom stress. Thus, usage of a constant, observed or literature-based C_D, is recommended but should be calibrated to account for inaccuracies in modeled currents.

Using the observed ε and scaling the bottom stress according to the log-law (τ_L) captured turbulence-driven resuspension events when the mean-shear was low. Although sub-grid-scale turbulent fluctuations driving resuspension (e.g, w') are not reproduced in RANS models, the log-law parameterization should be further tested and improved by better parameterization of ε to allow for simulation of resuspension associated with localized turbulence from wave breaking or convection.

Data and Code Availability Statement

Data and code used in this study are available at https://doi.org/10.5281/zenodo.7391269 . The Zenodo archive contains observed current, wind, and turbidity data, and scripts used to process bottom shear stress, as well as model setups and outputs from AEM3D model. The AEM3D executable is available for a nominal license fee from HydroNumerics (https://www.hydronumerics.com.au/ , last access: December 2022). The AEM3D source code was not modified in this application but is available with permission from HydroNumerics. ELCD model is not distributed anymore, but CAEDYM model is able to be coupled with

AEM3D to simulate the water quality. The CAEDYM executable is available within AEM3D package.

Reference

Aghsaee, P., & Boegman, L. (2015). Experimental investigation of sediment resuspension beneath internal solitary waves of depression. *Journal of Geophysical Research: Oceans, 120*(5), 3301-3314. doi: 10.1002/2014JC010401

Anderson, R. N., Hobart, M. A., & Langseth, M. G. (1979). Geothermal Convection Through Oceanic Crust and Sediments in the Indian Ocean. *Science, 204*(4395), 828-832. doi: 10.1126/science.204.4395.828

Austin, J. (2013). Observations of near-inertial energy in Lake Superior. *Limnology and Oceanography, 58*(2), 715-728. doi: 10.4319/lo.2013.58.2.0715

Bagnold, R. A. (1966). *An approach to the sediment transport problem from general physics*. Washington. US government printing office.

Barua, D. K. (2005). Wave Hindcasting. In M. L. Schwartz (Ed.), *Encyclopedia of Coastal Science. Encyclopedia of Earth Science Series.* Dordrecht: Springer.

Beletsky, D., Saylor, J. H., & Schwab, D. J. (1999). Mean Circulation in the Great Lakes. *Journal of Great Lakes Research, 25*(1), 78-93. doi: 10.1016/S0380-1330(99)70718-5

Biron, P. M., Robson, C., Lapointe, M. F., & Gaskin, S. J. (2004). Comparing different methods of bed shear stress estimates in simple and complex flow fields. *Earth Surface Processes and Landforms, 29*(11), 1403-1415. doi: 10.1002/esp.1111

Bluteau, C., Smith, S., Ivey, G., Schlosser, T., & Jones, N. (2016). *Assessing the relationship between bed shear stress estimates and observations of sediment resuspension in the ocean.* Paper presented at the 20th Australasian Fluid Mechanics Conference.

Boegman, L., Imberger, J., Ivey, G. N., & Antenucci, J. P. (2003). High-frequency internal waves in large stratified lakes. *Limnology and Oceanography, 48*(2), 895-919. doi: 10.4319/lo.2003.48.2.0895

Boegman, L., & Ivey, G. N. (2009). Flow separation and resuspension beneath shoaling nonlinear internal waves. *Journal of Geophysical Research: Oceans, 114*(C2). doi: 10.1029/2007JC004411

Boegman, L., Loewen, M. R., Hamblin, P. F., & Culver, D. A. (2001). Application of a two-dimensional hydrodynamic reservoir model to Lake Erie. *Canadian Journal of Fisheries and Aquatic Sciences, 58*(5), 858-869. doi:10.1139/f01-035

Boegman, L., & Stastna, M. (2019). Sediment Resuspension and Transport by Internal Solitary Waves. *Annual Review of Fluid Mechanics, 51*(1), 129-154. doi:10.1146/annurev-fluid-122316-045049

Boudreau, B. P., & Jorgensen, B. B. (2001). The benthic boundary layer: Transport processes and biogeochemistry. New York. Oxford University Press. Inc.

Bouffard, D., Ackerman, J. D., & Boegman, L. (2013). Factors affecting the development and dynamics of hypoxia in a large shallow stratified lake: Hourly to seasonal patterns. *Water Resources Research, 49*(5), 2380-2394. doi: 10.1002/wrcr.20241

Bouffard, D., Boegman, L., Ackerman, J. D., Valipour, R., & Rao, Y. R. (2014). Near-inertial wave driven dissolved oxygen transfer through the thermocline of a large lake. *Journal of Great Lakes Research, 40*(2), 300-307. doi: 10.1016/j.jglr.2014.03.014

Bouffard, D., Boegman, L., & Rao, Y. R. (2012). Poincaré wave–induced mixing in a large lake. *Limnology and Oceanography, 57*(4), 1201-1216. doi: 10.4319/lo.2012.57.4.1201

Bourgault, D., Morsilli, M., Richards, C., Neumeier, U., & Kelley, D. E. (2014). Sediment resuspension and nepheloid layers induced by long internal solitary waves shoaling orthogonally on uniform slopes. *Continental Shelf Research, 72*, 21-33. doi: 10.1016/j.csr.2013.10.019

Bruton M.N. (1985) The effects of suspensoids on fish. In: Davies B.R., Walmsley R.D. (eds) Perspectives in Southern Hemisphere Limnology. Developments in Hydrobiology, vol 28. Springer, Dordrecht. doi: 10.1007/978-94-009-5522-6_16

Churchill, J. H., Williams, A. J., & Ralph, E. A. (2004). Bottom stress generation and sediment transport over the shelf and slope off of Lake Superior's Keweenaw peninsula. *Journal of Geophysical Research: Oceans, 109*(C10). doi: 10.1029/2003JC001997

Donohue, I., & Garcia Molinos, J. (2009). Impacts of increased sediment loads on the ecology of lakes. *Biological Reviews, 84*(4), 517-531. doi: 10.1111/j.1469-185X.2009.00081.x

Fukuda, M. K., & Lick, W. (1980). The entrainment of cohesive sediments in freshwater. *Journal of Geophysical Research: Oceans, 85*(C5), 2813-2824. doi: 10.1029/JC085iC05p02813

Haltuch, M. A., Berkman, P. A., & Garton, D. W. (2000). Geographic information system (GIS) analysis of ecosystem invasion: Exotic mussels in Lake Erie. *Limnology and Oceanography, 45*(8), 1778-1787. doi: 10.4319/lo.2000.45.8.1778

Hawley, N., & Eadie, B. J. (2007). Observations of Sediment Transport in Lake Erie during the Winter of 2004–2005. *Journal of Great Lakes Research, 33*(4), 816-827. doi: 10.3394/0380-1330(2007)33[816:OOSTIL]2.0.CO;2

Hawley, N., Lesht, B. M., & Schwab, D. J. (2004). A comparison of observed and modeled surface waves in southern Lake Michigan and the implications for models of sediment resuspension. *Journal of Geophysical Research: Oceans, 109*(C10). doi: 10.1029/2002JC001592

Hawley, N., Wang, X., Brownawell, B., & Flood, R. (1996). Resuspension of Bottom Sediments in Lake Ontario During the Unstratified Period, 1992–1993. *Journal of Great Lakes Research, 22*(3), 707-721. doi: 10.1016/S0380-1330(96)70991-7

Hodges, B. R., Imberger, J., Saggio, A., & Winters, K. B. (2000). Modeling basin-scale internal waves in a stratified lake. *Limnology and Oceanography, 45*(7), 1603-1620. doi: 10.4319/lo.2000.45.7.1603

Hu, K., Ding, P., Wang, Z., Yang, S. (2009). A 2D/3D hydrodynamic and sediment transport model for the Yangtze Estuary, China. *Journal of Marine Systems, 77*(1), 114-136. doi: 10.1016/j.jmarsys.2008.11.014

Jabbari, A., Boegman, L., & Piomelli, U. (2015). Evaluation of the inertial dissipation method within boundary layers using numerical simulations. *Geophysical Research Letters, 42*(5), 1504-1511. doi:10.1002/2015GL063147

Jabbari, A., Boegman, L., Valipour, R., Wain, D., & Bouffard, D. (2020). Dissipation of Turbulent Kinetic Energy in the Oscillating Bottom Boundary Layer of a Large Shallow Lake. *Journal of Atmospheric and Oceanic Technology, 37*(3), 517-531. doi:10.1175/jtech-d-19-0083.1

Jonsson, I. G. (1966). Wave Boundary Layers and Friction Factors. In *Coastal Engineering 1966* (pp. 127-148).

Johnson, B. A., & Cowen, E. A. (2020). Sediment suspension and bed morphology in a mean shear free turbulent boundary layer. *Journal of Fluid Mechanics, 894*, A8. doi:10.1017/jfm.2020.222

Kim, S.-C., Friedrichs, C. T., Maa, J. P.-Y., & Wright, L. D. (2000). Estimating Bottom Stress in Tidal Boundary Layer from Acoustic Doppler Velocimeter Data. *Journal of Hydraulic Engineering, 126*(6), 399-406. doi: 10.1061/(ASCE)0733-9429(2000)126:6(399)

León, L. F., Imberger, J., Smith, R. E. H., Hecky, R. E., Lam, D. C. L., & Schertzer, W. M. (2005). Modeling as a Tool for Nutrient Management in Lake Erie: a Hydrodynamics Study. *Journal of Great Lakes Research, 31*, 309-318. doi: 10.1016/S0380-1330(05)70323-3

Lick, W., Lick, J., & Kirk Ziegler, C. (1994). The Resuspension and Transport of Fine-Grained Sediments in Lake Erie. *Journal of Great Lakes Research, 20*(4), 599-612. doi: 10.1016/S0380-1330(94)71181-3

Lin, S., Boegman, L., & Rao, Y. R. (2021a). Characterizing spatial and temporal distributions of turbulent mixing and dissipation in Lake Erie. *Journal of Great Lakes Research, 47*(1), 168-179. doi:10.1016/j.jglr.2020.11.014

Lin, S., Boegman, L., Valipour, R., Bouffard, D., Ackerman, J. D., & Zhao, Y. (2021b). Three-dimensional modeling of sediment resuspension in a large shallow lake. *Journal of Great Lakes Research, 47*(4), 970-984. doi: 10.1016/j.jglr.2021.04.014

Liu, W., Bocaniov, S. A., Lamb, K. G., & Smith, R. E. H. (2014). Three dimensional modeling of the effects of changes in meteorological forcing on the thermal structure of Lake Erie. *Journal of Great Lakes Research, 40*(4), 827-840. doi: 10.1016/j.jglr.2014.08.002

Lohrmann, A. (2001). Monitoring sediment concentration with acoustic backscattering instruments. *Nortek Technical Note, 3*, 1-5.

Lorke, A. (2007). Boundary mixing in the thermocline of a large lake. *Journal of Geophysical Research: Oceans, 112*(C9). doi: 10.1029/2006JC004008

Lou, J., Schwab, D. J., Beletsky, D., & Hawley, N. (2000). A model of sediment resuspension and transport dynamics in southern Lake Michigan. *Journal of Geophysical Research: Oceans, 105*(C3), 6591-6610. doi: 10.1029/1999JC900325

McGinnis, D. F., Sommer, S., Lorke, A., Glud, R. N., & Linke, P. (2014). Quantifying tidally driven benthic oxygen exchange across permeable sediments: An aquatic eddy correlation study. *Journal of Geophysical Research: Oceans, 119*(10), 6918-6932. doi: 10.1002/2014JC010303

Morales-Marin, L. A., French, J. R., Burningham, H., & Battarbee, R. W. (2018). Three-dimensional hydrodynamic and sediment transport modeling to test the sediment focusing hypothesis in upland lakes. *Limnology and Oceanography, 63*(S1), S156-S176. doi: 10.1002/lno.10729

Niu, Q., Xia, M., Ludsin, S. A., Chu, P. Y., Mason, D. M., & Rutherford, E. S. (2018). High-turbidity events in Western Lake Erie during ice-free cycles: Contributions of river-loaded vs. resuspended sediments. *Limnology and Oceanography, 63*(6), 2545-2562. doi: 10.1002/lno.10959

Paerl, H. W., Hall, N. S., & Calandrino, E. S. (2011). Controlling harmful cyanobacterial blooms in a world experiencing anthropogenic and climatic-induced change. *Science of The Total Environment, 409*(10), 1739-1745. doi: 10.1016/j.scitotenv.2011.02.001

Pope, S. B. (2000). *Turbulent Flows*. Cambridge, U.K.: Cambridge Univ. Press.

Quaresma, L. S., Vitorino, J., Oliveira, A., & da Silva, J. (2007). Evidence of sediment resuspension by nonlinear internal waves on the western Portuguese mid-shelf. *Marine Geology, 246*(2), 123-143. doi: 10.1016/j.margeo.2007.04.019

Rao, Y. R., Hawley, N., Charlton, M. N., & Schertzer, W. M. (2008). Physical processes and hypoxia in the central basin of Lake Erie. *Limnology and Oceanography, 53*(5), 2007-2020. doi: 10.4319/lo.2008.53.5.2007

Salim, S., Pattiaratchi, C., Tinoco, R. O., & Jayaratne, R. (2018). Sediment Resuspension Due to Near-Bed Turbulent Effects: A Deep Sea Case Study on the Northwest Continental Slope of Western Australia. *Journal of Geophysical Research: Oceans, 123*(10), 7102-7119. doi: 10.1029/2018JC013819

Sheng, Y. P., & Lick, W. (1979). The transport and resuspension of sediments in a shallow lake. *Journal of Geophysical Research: Oceans, 84*(C4), 1809-1826. doi: 10.1029/JC084iC04p01809

Shields, A. F. (1936). Application of similarity principles and turbulence research to bed-load movement. Pasadeza, California. California Institute of Technology.

Soulsby, R. L., Atkins, R., & Salkield, A. P. (1994). Observations of the turbulent structure of a suspension of sand in a tidal current. *Continental Shelf Research, 14*(4), 429-435. doi: 10.1016/0278-4343(94)90027-2

Soulsby, R. L. (1983). Chapter 5 The Bottom Boundary Layer of Shelf Seas. In B. Johns (Ed.), *Elsevier Oceanography Series* (Vol. 35, pp. 189-266): Elsevier.

Soulsby, R. L., & Whitehouse, R. J. S. (1997). *Threshold of sediment motion in coastal environments.* Paper presented at the Proceedings of the 13th Australasian Coastal and Ocean Engineering Conference and the 6th Australasian Port and Harbour Conference.

Spigel, R. H., Imberger, J., & Rayner, K. N. (1986). Modeling the diurnal mixed layer. *Limnology and Oceanography, 31*(3), 533-556. doi: 10.4319/lo.1986.31.3.0533

Stapleton, K. R., & Huntley, D. A. (1995). Seabed stress determinations using the inertial dissipation method and the turbulent kinetic energy method. *Earth Surface Processes and Landforms, 20*(9), 807-815. doi: 10.1002/esp.3290200906

Valipour, R., Boegman, L., Bouffard, D., & Rao, Y. R. (2017). Sediment resuspension mechanisms and their contributions to high-turbidity events in a large lake. *Limnology and Oceanography, 62*(3), 1045-1065. doi: 10.1002/lno.10485

Valipour, R., Bouffard, D., & Boegman, L. (2015a). Parameterization of bottom mixed layer and logarithmic layer heights in central Lake Erie. *Journal of Great Lakes Research, 41*(3), 707-718. doi: 10.1016/j.jglr.2015.06.010

Valipour, R., Bouffard, D., Boegman, L., & Rao, Y. R. (2015). Near-inertial waves in Lake Erie. *Limnology and Oceanography, 60*(5), 1522-1535. doi: 10.1002/lno.10114

Van Rijn, L. C. (1990). *Principles of Fluid Flow and Surface Waves in Rivers, Estuaries, Seas and Oceans* (Vol. 12). Amsterdam: Aqua Publications.

Van Rijn, L. C. (1993). *Principles of Sediment Transport in Rivers, Estuaries and Coastal Seas* (Vol. 1006). Amsterdam: Aqua publications.

Voulgaris, G., & Trowbridge, J. H. (1998). Evaluation of the Acoustic Doppler Velocimeter (ADV) for Turbulence Measurements*. *Journal of Atmospheric and Oceanic Technology, 15*(1), 272-289. doi:10.1175/1520-0426(1998)015<0272:EOTADV>2.0.CO;2

Warner, J. C., Sherwood, C. R., Signell, R. P., Harris, C. K., & Arango, H. G. (2008). Development of a three-dimensional, regional, coupled wave, current, and sediment-transport model. *Computers & Geosciences, 34*(10), 1284-1306. doi: 10.1016/j.cageo.2008.02.012

Yang, Y., Wang, Y. P., Gao, S., Wang, X. H., Shi, B. W., Zhou, L., Wang, D. D., Dai, C., & Li, G. C. (2016). Sediment resuspension in tidally dominated coastal environments: new insights into the threshold for initial movement. *Ocean Dynamics, 66*(3), 401-417. doi:10.1007/s10236-016-0930-6

Yuan, Y., Wei, H., Zhao, L., & Cao, Y. (2009). Implications of intermittent turbulent bursts for sediment resuspension in a coastal bottom boundary layer: A field study in the western Yellow Sea, China. *Marine Geology, 263*(1), 87-96. doi: 10.1016/j.margeo.2009.03.023

Zulberti, A. P., Ivey, G. N., & Jones, N. L. (2018). *Observations of near-bed stress beneath nonlinear internal wave trains in the ocean.* Paper presented at the 21st Australasian Fluid Mechanics Conference, Adelaide, Austrilia.

Fig. 1. (a) Map of Lake Erie showing the location of field observation (Sta. 341) and National Data Buoy Center (NDBC) wave buoy (45005). Negative numbers show the depth contours in meters. Red triangles are the sources of meteorological data used to drive the AEM3D and ELCOM models. (b) The tripod equipped with ADCPs, an ADV and RBR TR-1060s before deployment on the lakebed at Sta. 341 in 2008. (c) West-to-east curtain showing vertical grid (z-level) spacing in the models.

Fig. 2. Time-series at Sta. 341 for 2008 (a) wind speed (blue line; left y-axis) and direction (red dashed line; right y-axis) at 10 m above water surface, (b) turbidity at 1.5 mab from XR-620 (black stars) and its 7-day moving mean (grey line) and 7-day standard deviation (grey shading), (c) ADV-amp at 1 mab (blue dots) and its 7-day moving mean (blue line) and 7-day standard deviation (blue shading), (d) τ_L (purple dash-dot line, Eq. 10), τ_{TKE} (green dash-dot line, Eq. 5) and critical value for resuspension (τ_{cr}=0.045 Pa; black dashed line), (e) τ_w (blue line, Eq. 6), τ_c (red line, Eq. 9) and τ_{cr}, (f-h) Modeled $\tau_{c,m}$ and $\tau_{w,m}$ based on varying C_D and algorithms.

Fig. 3. Time-series at Sta. 341 for first deployment in 2009 (a) wind speed (blue line; left y-axis) and direction (red dashed line; right y-axis) at 10 m above water surface, (b) turbidity at 1.5 mab from XR-620 (black stars) and its 7-day moving mean (grey line) and standard deviation (grey shading) (left y-axis). Green stars are *Chl-a* concentration at 5 mab from XR-420 (right y-axis), (c) ADV-amp at 1 mab (blue dots) and its 7-day moving mean (blue line) and standard deviation (blue shading). Color bar shows the ADCP echo level, (d) τ_L (purple dash-dot line, Eq. 10), τ_{TKE} (green dash-dot line, Eq. 5) and τ_{cr} (black dashed line), (e) τ_w (blue line, Eq. 6), τ_c (red line, Eq. 9) and τ_{cr}, (f-g) Modeled $\tau_{c,m}$ and $\tau_{w,m}$ based on the algorithms in AEM3D with varying C_D (h) Modeled $\tau_{c,m}$ and $\tau_{w,m}$ based on the algorithms in ELCD.

Fig. 4. Time-series at Sta. 341 for second deployment in 2009 (a) wind speed (blue line; left y-axis) and direction (red dashed line; right y-axis) at 10 m above water surface, (b) turbidity at 1.5 mab from XR-620 (black stars) and its 7-day moving mean (grey line) and standard deviation (grey shading), and green shading indicates the high turbidity from algae (Paerl et al., 2011), (c) ADV-amp at 1 mab (blue dots) and its 7-day moving mean (blue line) and standard deviation (blue shading), (d) τ_L (purple dash-dot line, Eq. 10), τ_{TKE} (green dash-dot line, Eq. 5) and τ_{cr} (black dashed line), (e) τ_w (blue line, Eq. 6), τ_c (red line, Eq. 9) and τ_{cr}, (f-g) Modeled $\tau_{c,m}$ and $\tau_{w,m}$ based on the algorithms in AEM3D with varying C_D (h) Modeled $\tau_{c,m}$ and $\tau_{w,m}$ based on the algorithms in ELCD.

Fig. 5 Details of resuspension events R21-23 in Fig. 4. Time-series at Sta. 341 of (a-c) wind speed (blue lines; left y-axis) and direction (red dashed lines; right y-axis) at 10 m above water surface, (b-f) turbidity at 1.5 mab from XR-620 (black stars) and its 7-day moving mean (grey line) and standard deviation (grey shading), (g-i) ADV-amp at 1 mab (right y-axis), and its 7-day moving mean (blue line) and standard deviation (blue shading), (j-l) show τ_{TKE} (purple dash-dot line, Eq. 5) and τ_L (green dash-dot line, Eq. 10) based on turbulent velocity from ADV, and *in situ* critical value for resuspension τ_{cr} = 0.045 Pa, (m-o) τ_w (blue line, Eq. 6) based NDBC station 45005, τ_c (red line,

Eq. 9) based on mean current velocity from ADV, and τ_{cr} (black dashed line), (p-r) AEM3D output $\tau_{w,m}$ (blue dotted line) and $\tau_{c,m}$ (red dotted line) used C_D = 0.0024, (s-u) AEM3D output $\tau_{w,m}$ (blue dashed line) and $\tau_{c,m}$ (red dashed line) used C_D = 0.0045; and (v-x) are ELCD output $\tau_{w,m}$ (blue dashed line) and $\tau_{c,m}$ (red dashed line).

Fig. 6 Details of resuspension events R14, 15, 17 in Fig. 3. Time-series at Sta. 341 of (a-c) wind speed (blue lines; left y-axis) and direction (red dashed lines; right y-axis) at 10 m above water surface, (b-f) turbidity at 1.5 mab from XR-620 (black stars) and its 7-day moving mean (grey line) and standard deviation (grey shading), green shading indicates the high turbidity from algae (Paerl et al., 2011), (g-i) ADV-amp at 1 mab (right y-axis), and its 7-day moving mean (blue line) and standard deviation (blue shading), (j-l) show τ_{TKE} (purple dash-dot line, Eq. 5) and τ_L (green dash-dot line, Eq. 10) based on turbulent velocity from ADV, and *in situ* critical value for resuspension τ_{cr} = 0.045 Pa, (m-o) τ_w (blue line, Eq. 6) based NDBC station 45005, τ_c (red line, Eq. 9) based on mean current velocity from ADV, and τ_{cr} (black dashed line), (p-r) AEM3D output $\tau_{w,m}$ (blue dotted line) and $\tau_{c,m}$ (red dotted line) used C_D = 0.0024; (s-u) AEM3D output $\tau_{w,m}$ (blue dashed line) and $\tau_{c,m}$ (red dashed line) used C_D = 0.0045, and (v-x) are ELCD output $\tau_{w,m}$ (blue dashed line) and $\tau_{c,m}$ (red dashed line).

Fig. 7 Details of resuspension events R7, 10, 12 in Fig. 2, 3. Time-series at Sta. 341 of (a-c) wind speed (blue lines; left y-axis) and direction (red dashed lines; right y-axis) at 10 m above water surface, (b-f) turbidity at 1.5 mab from XR-620 (black stars) and its 7-day moving mean (grey line) and standard deviation (grey shading), and Chl-a concentration at 5 mab from XR-420 (right y-axis), (g-i) ADV-amp at 1 mab (right y-axis), its 7-day moving mean (blue line) and standard deviation (blue shading), and colorbar shows the ADCP echo level; (j-l) show τ_{TKE} (purple dash-dot line, Eq. 5) and τ_L (green dash-dot line, Eq. 10) based on turbulent velocity from ADV, and *in situ* critical value for resuspension (τ_{cr} = 0.045 Pa; black dashed line); (m-o) τ_w (blue line, Eq. 6) based NDBC station 45005, τ_c (red line, Eq. 9) based on mean current velocity from ADV, and τ_{cr} (black dashed line); (p-r) AEM3D output $\tau_{w,m}$ (blue dotted line) and $\tau_{c,m}$ (red dotted line) used C_D = 0.0024; (s-u) AEM3D output $\tau_{w,m}$ (blue dashed line) and $\tau_{c,m}$ (red dashed line) used C_D = 0.0045; and (v-x) are ELCD output $\tau_{w,m}$ (blue dashed line) and $\tau_{c,m}$ (red dashed line).

Fig. 8 Details of resuspension events R6 in Fig. 2. Time-series at Sta. 341 of 2008 (a) wind speed (left y-axis) and direction (right y-axis) at 10 m above water surface, (b) temperature contours from TR-1060 temperature loggers, red arrows show vertical locations of temperature loggers, (c) turbidity at 1.5 mab from XR-620 (left y-axis), and ADV-amp at 1 mab (right y-axis); (d) and (e) show τ_L (green dash-dot line, Eq. 10), τ_{TKE} (purple dash-dot line, Eq. 5), τ_w (blue line, Eq. 6), τ_c (red line, Eq. 9) based on observd data and τ_{cr} (black dashed line); (f) and (g) are ELCD output of temperature and TSS concentration at Sta. 341, respectively.

Fig. 9 Time-series at Sta. 341 of τ_L (Eq. 11) based on ε_m (Eq. 16, orange line) and ε_{ID} (green dash-dot line). Comparisons of observed and modelled turbulent dissipation are shown in Fig. S6.

Fig. 10 Mean value of AEM3D modeled $\tau_{w,m}$, $\tau_{c,m}$, and τ_b (a-c) over spring and summer (days 203 – 245 of 2008 and days 119- 250 of 2009), and (d-f) over fall (days 245- 303 of 2008 and days 250 – 300 of 2009).

Table 1 Assessment of bottom stress parameterization in ELCD (denoted by m1) and AEM3D (denoted by m2, 3) models.

Table 2 Parameterizations for τ_c in different sediment models. The equations in column 2 were solved using parameters characteristic to Lake Erie (column 4).

Figure 1.

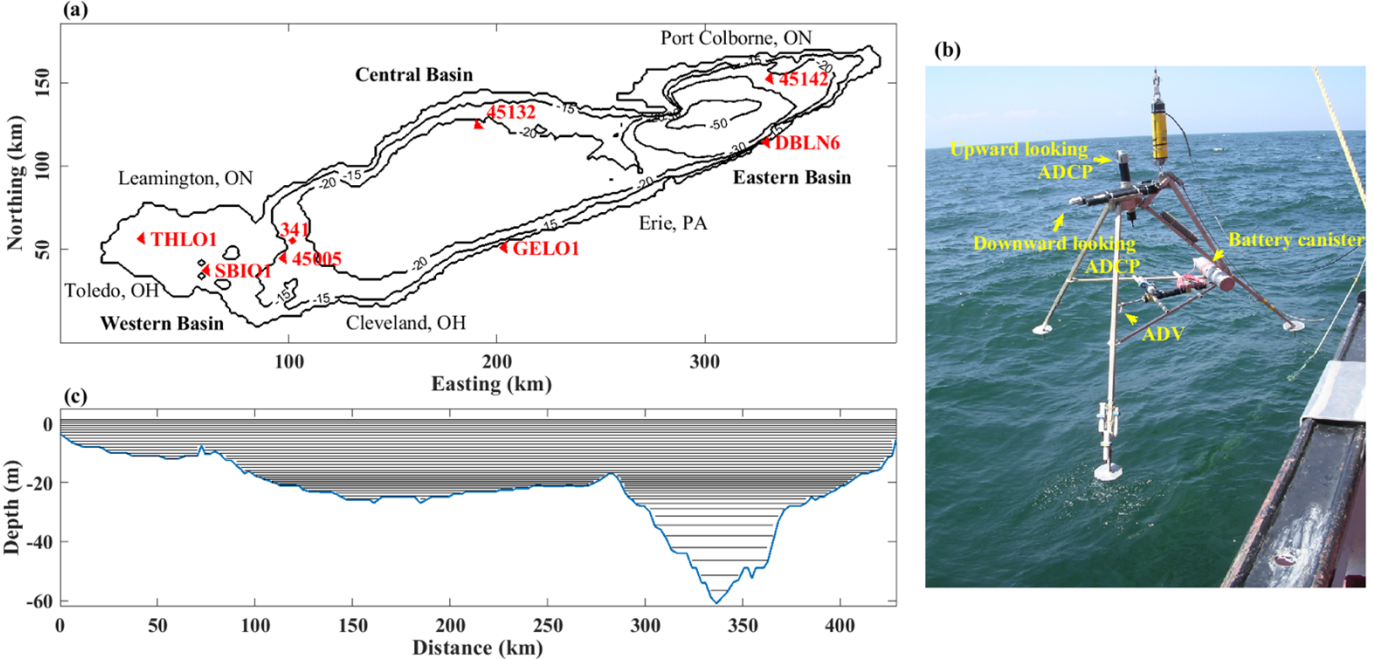
(a)
Port Colborne, ON
Central Basin
45142
45132
DBLN6
Leamington, ON
Eastern Basin
Erie, PA
341
THLO1
45005
GELO1
SBIO1
Toledo, OH
Western Basin
Cleveland, OH
Northing (km)
Easting (km)
(b)
Upward looking ADCP
Downward looking ADCP
Battery canister
ADV
(c)
Depth (m)
Distance (km)

Figure 2.

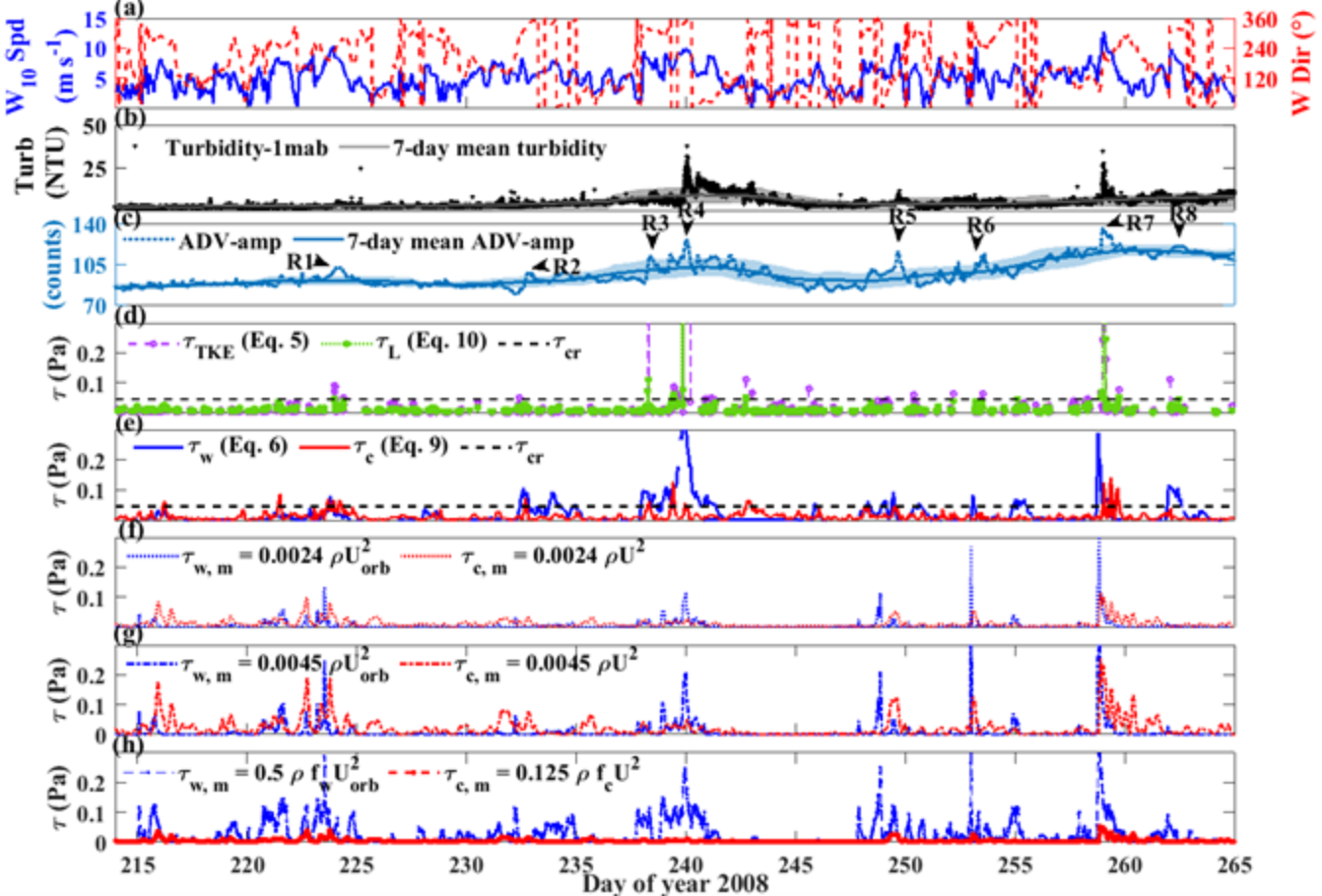
(a)
W_{10} Spd (m s^{-1})
W Dir (°)
(b)
Turb (NTU)
Turbidity-1mab
7-day mean turbidity
(c)
(counts)
ADV-amp
7-day mean ADV-amp
R1
R2
R3
R4
R5
R6
R7
R8
(d)
τ (Pa)
τ_{TKE} (Eq. 5)
τ_L (Eq. 10)
τ_{cr}
(e)
τ_w (Eq. 6)
τ_c (Eq. 9)
(f)
$\tau_{w,m} = 0.0024\ \rho U_{orb}^2$
$\tau_{c,m} = 0.0024\ \rho U^2$
(g)
$\tau_{w,m} = 0.0045\ \rho U_{orb}^2$
$\tau_{c,m} = 0.0045\ \rho U^2$
(h)
$\tau_{w,m} = 0.5\ \rho f_w U_{orb}^2$
$\tau_{c,m} = 0.125\ \rho f_c U^2$
Day of year 2008

Figure 3.

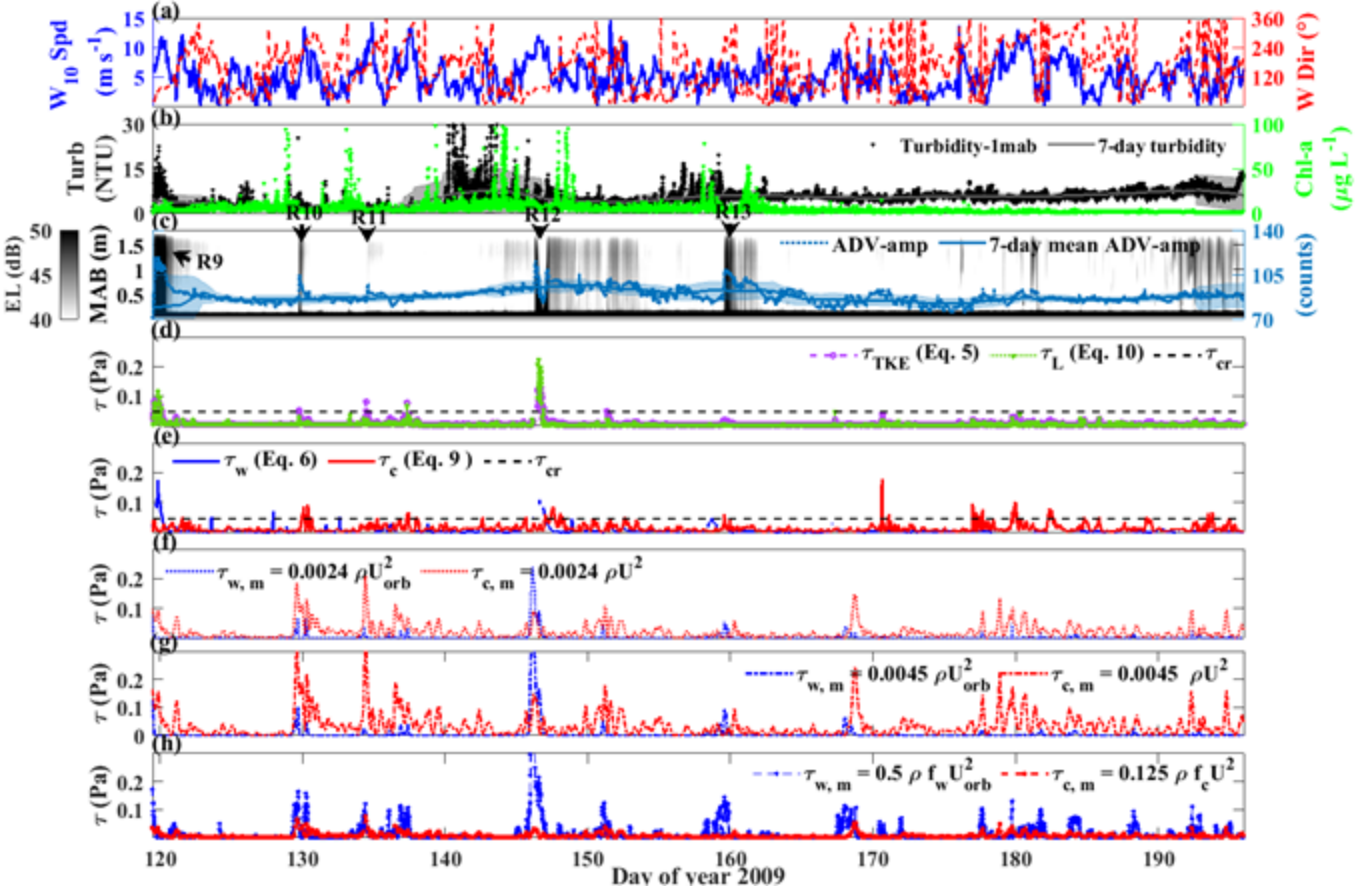
(a)
W10 Spd (m s-1)
W Dir (°)
(b)
Turb (NTU)
Turbidity-1mab
7-day turbidity
Chl-a (μg L-1)
(c)
EL (dB)
MAB (m)
R9
R10
R11
R12
R13
ADV-amp
7-day mean ADV-amp
(counts)
(d)
τ (Pa)
τTKE (Eq. 5)
τL (Eq. 10)
τcr
(e)
τw (Eq. 6)
τc (Eq. 9)
τcr
(f)
τw, m = 0.0024 ρU2orb
τc, m = 0.0024 ρU2
(g)
τw, m = 0.0045 ρU2orb
τc, m = 0.0045 ρU2
(h)
τw, m = 0.5 ρ fw U2orb
τc, m = 0.125 ρ fc U2
Day of year 2009

Figure 4.

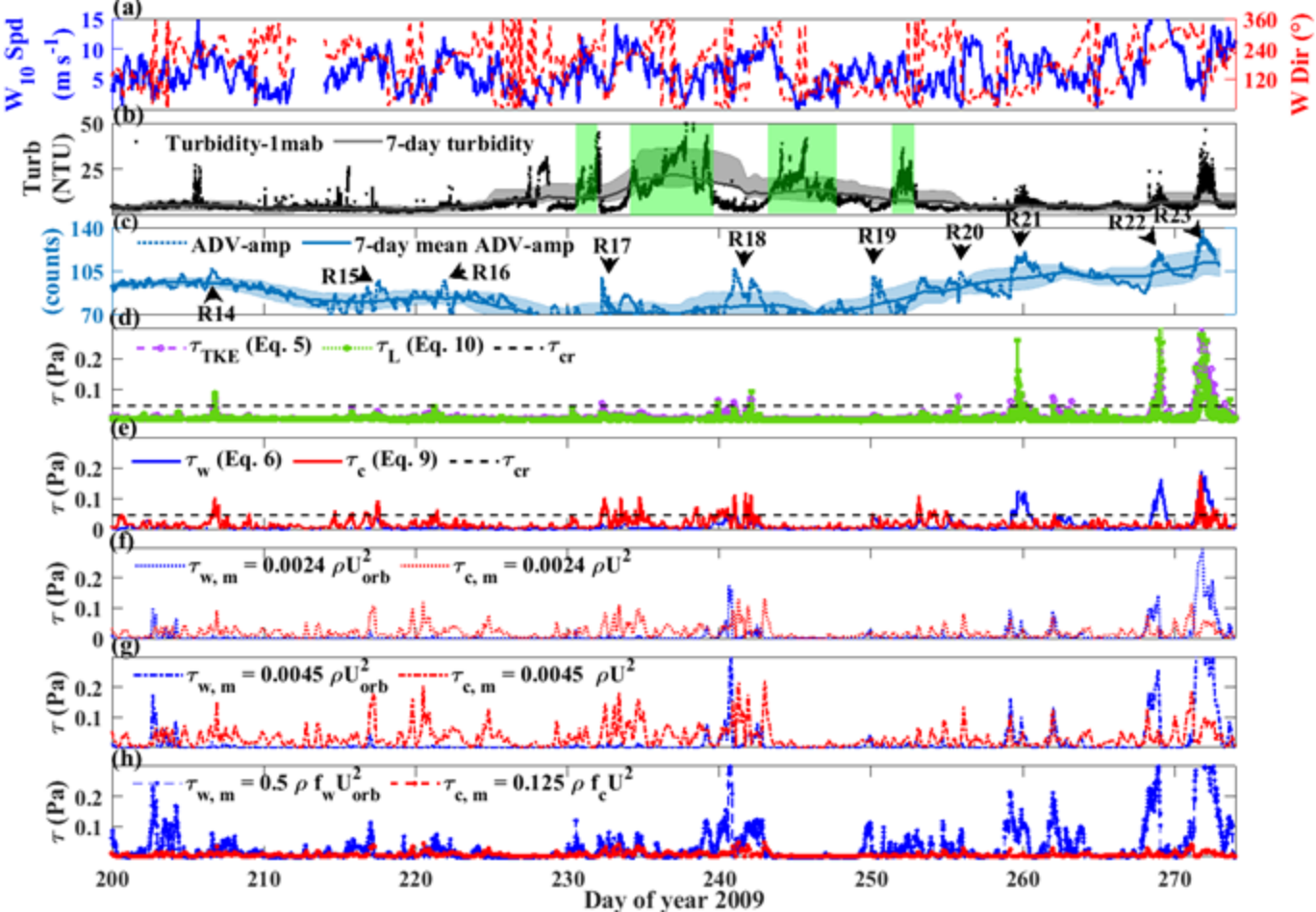
(a)
W_{10} Spd (m s^{-1})
W Dir (°)
(b)
Turb (NTU)
Turbidity-1mab
7-day turbidity
(c)
(counts)
ADV-amp
7-day mean ADV-amp
R14
R15
R16
R17
R18
R19
R20
R21
R22
R23
(d)
τ (Pa)
τ_{TKE} (Eq. 5)
τ_L (Eq. 10)
τ_{cr}
(e)
τ_w (Eq. 6)
τ_c (Eq. 9)
(f)
$\tau_{w,m} = 0.0024\ \rho U_{orb}^2$
$\tau_{c,m} = 0.0024\ \rho U^2$
(g)
$\tau_{w,m} = 0.0045\ \rho U_{orb}^2$
$\tau_{c,m} = 0.0045\ \rho U^2$
(h)
$\tau_{w,m} = 0.5\ \rho\ f_w U_{orb}^2$
$\tau_{c,m} = 0.125\ \rho\ f_c U^2$
Day of year 2009

Figure 5.

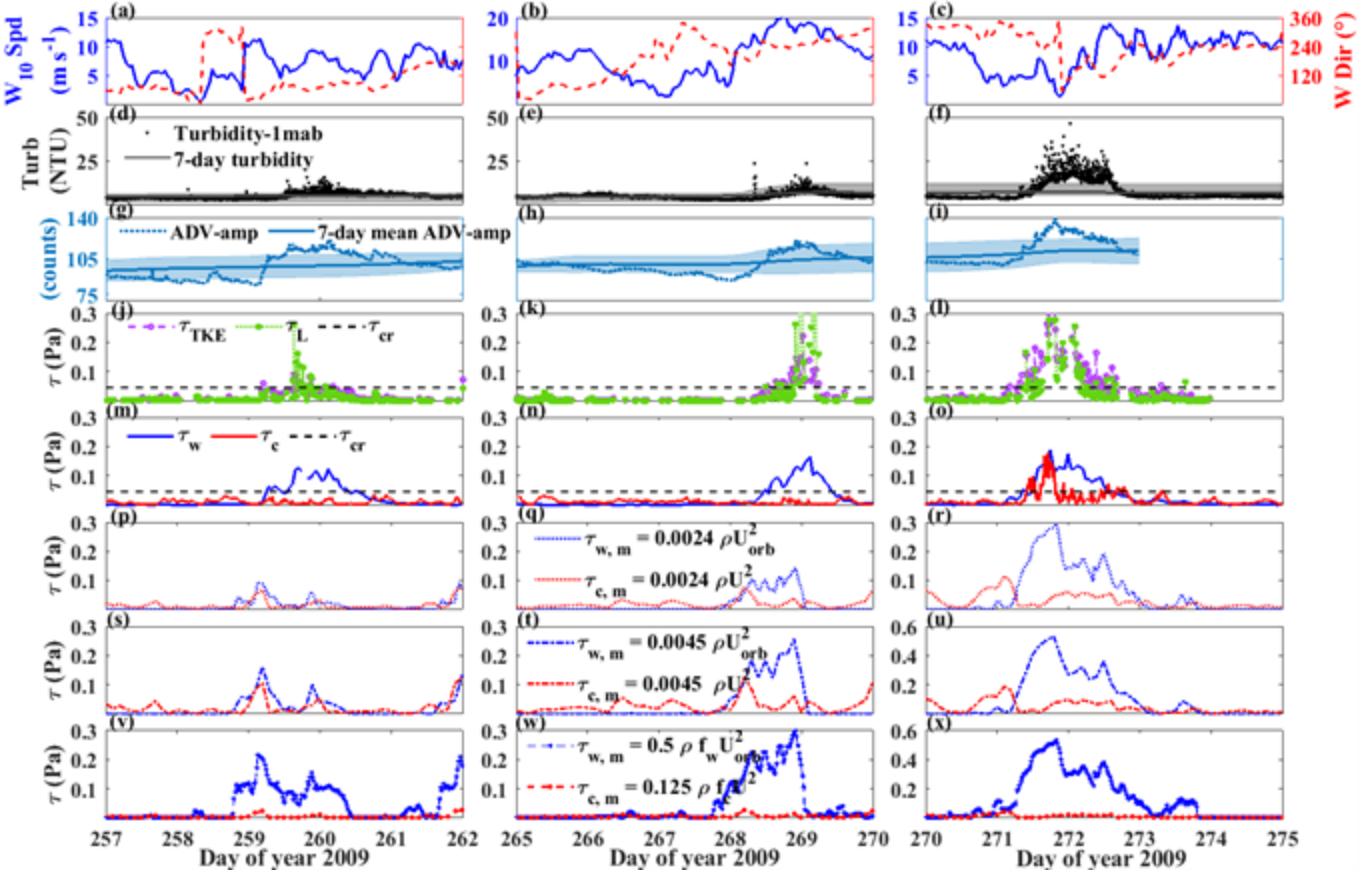
(a)
(b)
(c)
W_{10} Spd ($m\ s^{-1}$)
W Dir (°)
(d)
(e)
(f)
Turb (NTU)
Turbidity-1mab
7-day turbidity
(g)
(h)
(i)
(counts)
ADV-amp
7-day mean ADV-amp
(j)
(k)
(l)
τ (Pa)
τ_{TKE}
τ_L
τ_{cr}
(m)
(n)
(o)
τ_w
τ_c
τ_{cr}
(p)
(q)
(r)
$\tau_{w,m} = 0.0024\ \rho U_{orb}^2$
$\tau_{c,m} = 0.0024\ \rho U_{orb}^2$
(s)
(t)
(u)
$\tau_{w,m} = 0.0045\ \rho U_{orb}^2$
$\tau_{c,m} = 0.0045\ \rho U_{orb}^2$
(v)
(w)
(x)
$\tau_{w,m} = 0.5\ \rho\ f_w U_{orb}^2$
$\tau_{c,m} = 0.125\ \rho\ f_w U_{orb}^2$
Day of year 2009
Day of year 2009
Day of year 2009

Figure 6.

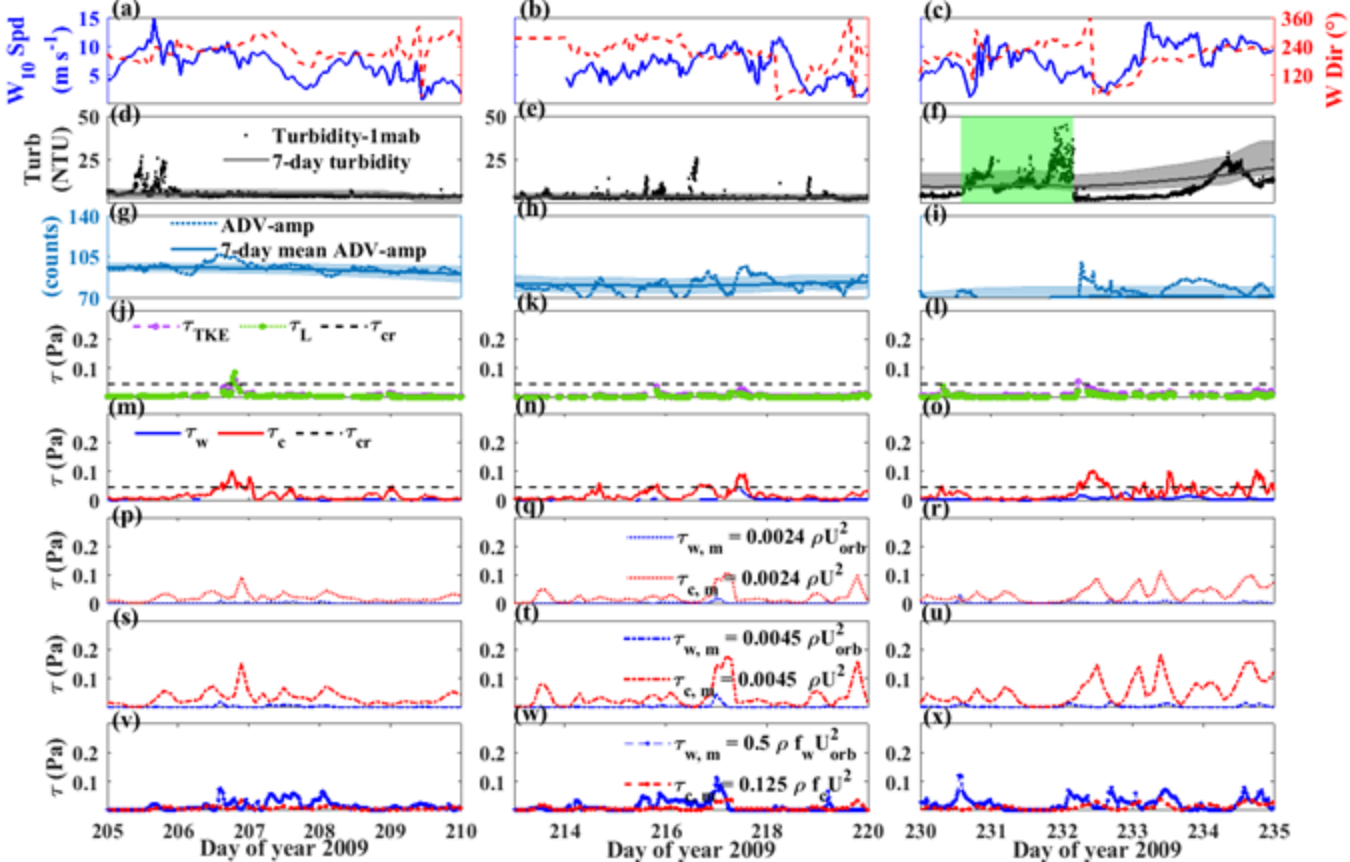
(a)
(b)
(c)
W_{10} Spd (m s^{-1})
W Dir (°)
(d)
(e)
(f)
Turb (NTU)
Turbidity-1mab
7-day turbidity
(g)
(h)
(i)
(counts)
ADV-amp
7-day mean ADV-amp
(j)
(k)
(l)
τ (Pa)
τ_{TKE}
τ_L
τ_{cr}
(m)
(n)
(o)
τ_w
τ_c
(p)
(q)
(r)
$\tau_{w,m} = 0.0024\ \rho U^2_{orb}$
$\tau_{c,m} = 0.0024\ \rho U^2$
(s)
(t)
(u)
$\tau_{w,m} = 0.0045\ \rho U^2_{orb}$
$\tau_{c,m} = 0.0045\ \rho U^2$
(v)
(w)
(x)
$\tau_{w,m} = 0.5\ \rho\ f_w U^2_{orb}$
$\tau_{c,m} = 0.125\ \rho\ f_c U^2$
Day of year 2009
Day of year 2009
Day of year 2009

Figure 7.

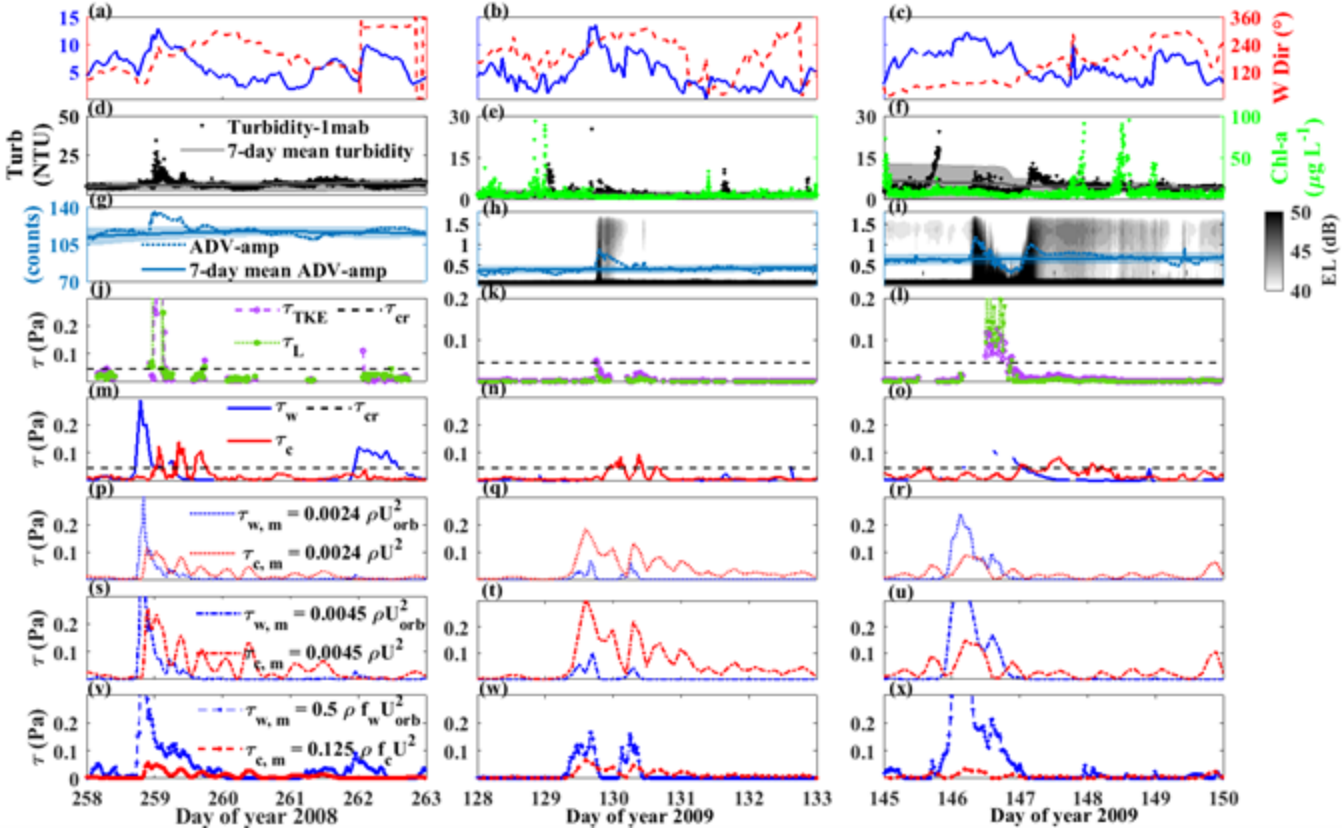
(a)
(b)
(c)
W Dir (°)
360
240
120
(d)
Turb (NTU)
Turbidity-1mab
7-day mean turbidity
(e)
(f)
Chl-a (μg L-1)
(g)
(counts)
ADV-amp
7-day mean ADV-amp
(h)
(i)
EL (dB)
(j)
τ (Pa)
τTKE
τcr
τL
(k)
(l)
(m)
τw
τc
(n)
(o)
(p)
τw, m = 0.0024 ρU2orb
τc, m = 0.0024 ρU2
(q)
(r)
(s)
τw, m = 0.0045 ρU2orb
τc, m = 0.0045 ρU2
(t)
(u)
(v)
τw, m = 0.5 ρ fwU2orb
τc, m = 0.125 ρ fcU2
(w)
(x)
Day of year 2008
Day of year 2009
Day of year 2009

Figure 8.

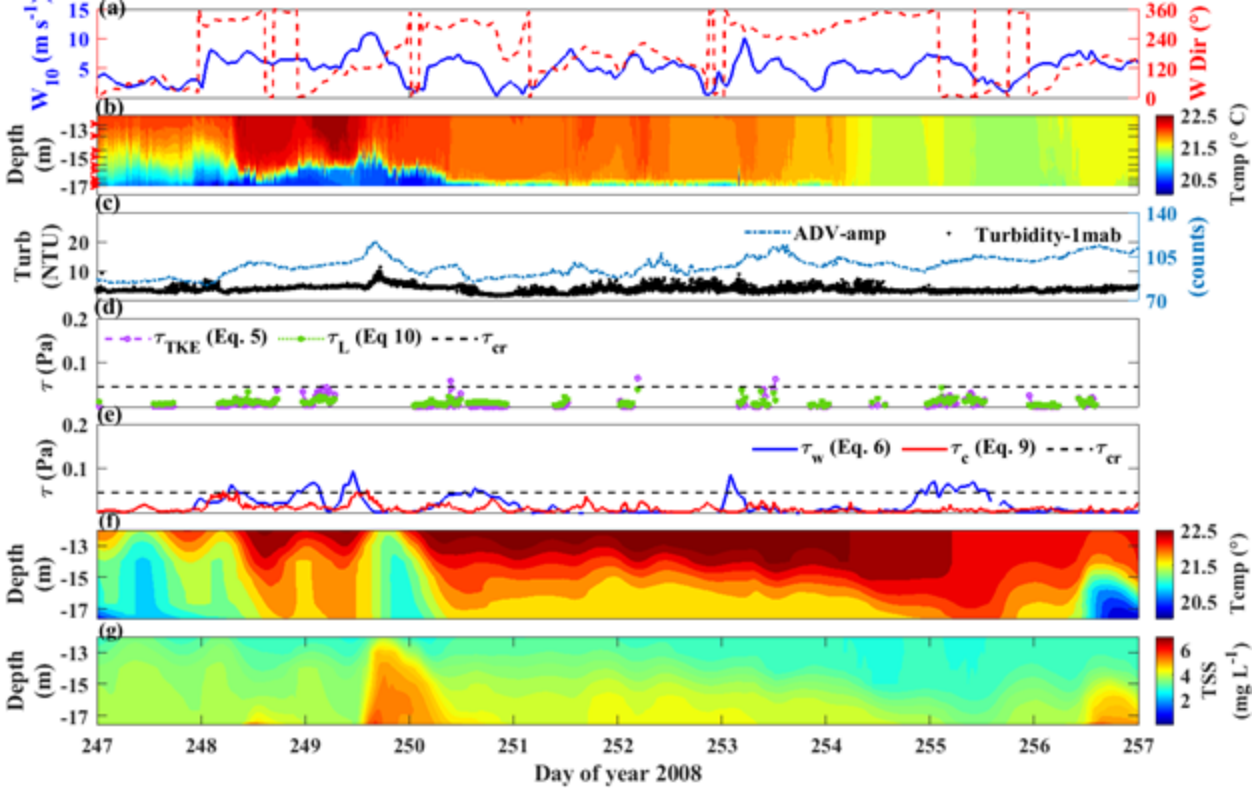
(a)
W_{10} (m s^{-1})
W Dir (°)
(b)
Depth (m)
Temp (° C)
(c)
Turb (NTU)
ADV-amp
Turbidity-1mab
(counts)
(d)
τ (Pa)
τ_{TKE} (Eq. 5)
τ_L (Eq 10)
τ_{cr}
(e)
τ (Pa)
τ_w (Eq. 6)
τ_c (Eq. 9)
τ_{cr}
(f)
Depth (m)
Temp (°)
(g)
Depth (m)
TSS (mg L^{-1})
Day of year 2008

Figure 9.

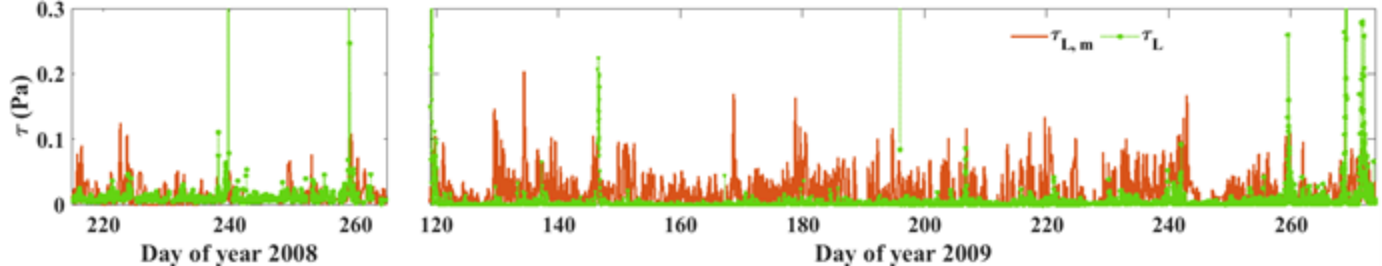
0.3
0.2
0.1
0
τ (Pa)
220
240
260
Day of year 2008
120
140
160
180
200
220
240
260
Day of year 2009
τL, m
τL

Figure 10.

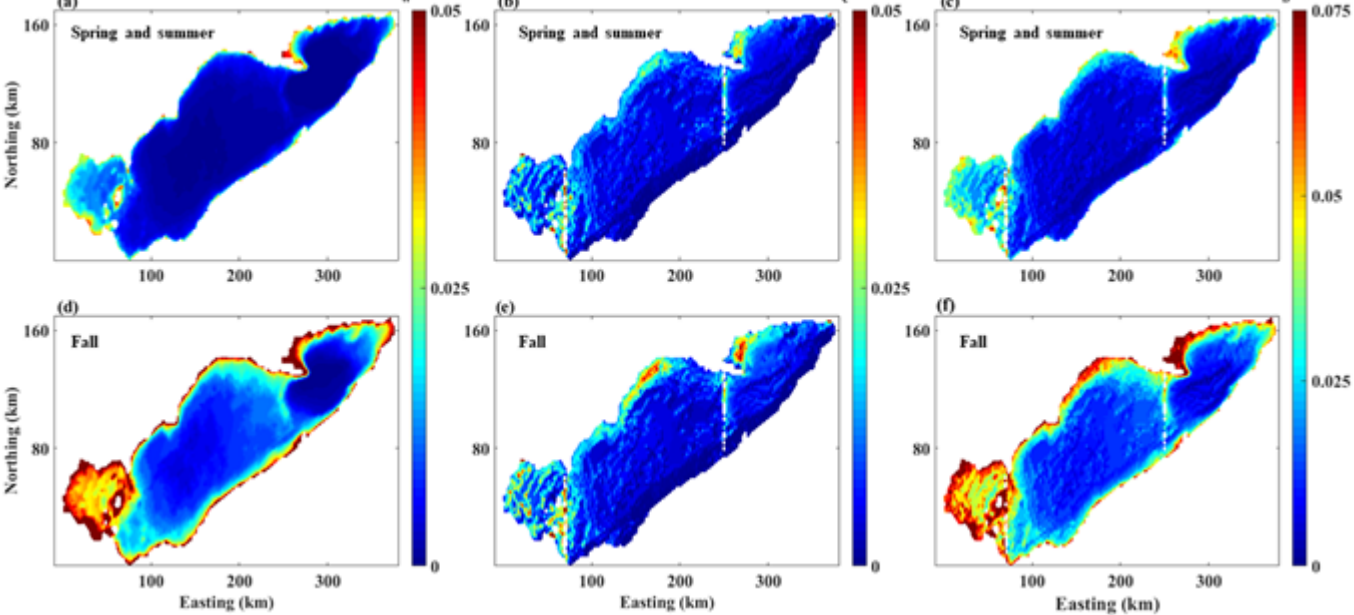
(a)
Spring and summer
(b)
Spring and summer
(c)
Spring and summer
(d)
Fall
(e)
Fall
(f)
Fall
τ_w (Pa)
τ_c (Pa)
τ_b (Pa)
0.05
0.025
0
0.075
0.05
0.025
0
Northing (km)
Easting (km)
160
80
100
200
300